Medical Image Analysis 72 (2021) 102088

Contents lists available at ScienceDirect

Medical Image Analysis

journal homepage: www.elsevier.com/locate/media

OFx: A method of 4D image construction from free-breathing non-gated MRI slice acquisitions of the thorax via optical flux

You Hao[a,b,d], Jayaram K. Udupa[b,*], Yubing Tong[b], Caiyun Wu[b], Hua Li[a,d], Joseph M. McDonough[c], Carina Lott[c], Catherine Qiu[c], Nirupa Galagedera[c], Jason B. Anari[c], Drew A. Torigian[b], Patrick J. Cahill[c]

[a] *Key Laboratory of Intelligent Information Processing, Institute of Computing Technology, Chinese Academy of Sciences, Beijing 100190, China*
[b] *Medical Image Processing Group, 602 Goddard building, 3710 Hamilton Walk, Department of Radiology, University of Pennsylvania, Philadelphia, PA 19104, USA*
[c] *Center for Thoracic Insufficiency Syndrome, Children's Hospital of Philadelphia, Philadelphia, PA 19104, USA*
[d] *University of Chinese Academy of Sciences, Beijing 100049, China*

ARTICLE INFO

Article history:
Received 12 December 2019
Revised 17 March 2021
Accepted 18 April 2021
Available online 25 April 2021

Keywords:
4D construction
Optical flux
Dynamic MRI
Respiratory signal extraction

ABSTRACT

Purpose: Since real-time 4D dynamic magnetic resonance imaging (dMRI) methods with adequate spatial and temporal resolution for imaging the pediatric thorax are currently not available, free-breathing slice acquisitions followed by appropriate 4D construction methods are currently employed. Self-gating methods, which extract breathing signals only from image information without any external gating technology, have much potential for this purpose, such as for use in studying pediatric thoracic insufficiency syndrome (TIS). Patients with TIS frequently suffer from extreme malformations of the chest wall, diaphragm, and spine, leading to breathing that is very complex, including deep or shallow respiratory cycles. Existing 4D construction methods cannot perform satisfactorily in this scenario, and most are not fully automatic, requiring manual interactive operations. In this paper, we propose a novel fully automatic 4D image construction method based on an image-derived concept called *flux* to address these challenges.

Methods: We utilized 25 dMRI data sets from 25 pediatric subjects with no known thoracic anomalies and 58 dMRI data sets from 29 patients with TIS where each patient had a dMRI scan before and after surgery. A time sequence of 80 slices are acquired at each sagittal location continuously at a rate of ~480 ms per slice under free-breathing conditions, with 30–40 sagittal locations across the chest for each subject depending on the thoracic size. In our approach, we first extract the breathing signal for each sagittal location based on the flux of the optical flow vector field of the body region from the image time series. Here, for each time point of respiratory phase, the net flux of the body region can be regarded as the flux going into or out of the body region, which we term Optical Flux (OFx). OFx provides a very robust representation of the real breathing motion of the thorax. OFx allows us to perform a full analysis of all respiratory cycles, extract only normal cycles in a robust manner, and map all extracted normal cycles on to one cosine respiration model for each sagittal location. Subsequently, we re-sample one normal cycle from the respiration model for each location independently. The normal cycle models associated with the different sagittal locations are finally composited to form the final constructed 4D image.

Results: We employ several metrics to evaluate the quality of the 4D construction results: E_{ie} – error in locating time instants corresponding to end inspiration and end expiration; E_{to} – deviation from correct temporal order in each detected normal cycle; E_{ss} – deviation in spatial smoothness; and E_{sc} – deviation from spatial continuity as scored by a reader. The means and standard deviations of these metrics for normal subjects and TIS patients are found to be, respectively: E_{ie}: 0.25 ± 0.05 and 0.38 ± 0.16 in units of time instance (ideal value = 0); E_{to}: 2.7% ± 2.3% and 1.8% ± 2% (ideal value = 0%); E_{ss}: 0.5 ± 0.17 and 0.54 ± 0.25 in pixel units (ideal value = 0); E_{sc}: 4.6 ± 0.48 and 4.56 ± 0.98 (score range: best = 5,

---

[*] Corresponding author.
E-mail address: jay@pennmedicine.upenn.edu (J.K. Udupa).

https://doi.org/10.1016/j.media.2021.102088

worst = 1). The results show that the OFx method achieves excellent spatial and temporal continuity and its yield was 100% meaning that it successfully performed 4D construction on every data set tested. Compared to a recently published method, OFx is fully automatic requiring about 5 min of computational time per study starting from acquired dMRI scans. The method achieves high temporal and spatial continuity even on complex TIS data sets that include many abnormal respiratory cycles.

Conclusions: A new 4D dMRI construction method based on the concept of optical flux is presented which is fully automatic and very robust in deriving respiratory signals purely from dynamic image sequences even when presented with complex breathing patterns due to severe disease conditions like TIS. Evaluations show that its accuracy is comparable to the variations found in manual annotations. An important characteristic of the method is that it is independent of the number of sagittal locations used in the construction process, which suggests that it is applicable to imaging techniques where data are acquired at only a few sagittal locations instead of the full width of the thorax. The method is not tied to any specific imaging modality, as demonstrated in this paper on not just dMRI but dynamic computed tomography (CT) as well.

Introduction

Respiratory organ motion analysis is important in the study of many disease processes (Crompton, 2006). In all such applications, a 4D image constituting the organ system under study over one respiratory cycle needs to be constructed first. Since the patient cooperation needed by gating or tracking techniques is often hard to achieve, such as in the case of pediatric patients or for patients who are mentally impaired or have severe malformations of the chest wall, diaphragm, and spine (Campbell Jr. et al., 2003; Campbell Jr. and Smith, 2007), high-quality, highly automated 4D imaging technology under free-breathing image acquisitions is becoming increasingly important in clinical applications. Compared to computed tomography (CT), magnetic resonance imaging (MRI) has three natural advantages: excellent soft tissue contrast, no ionizing radiation exposure, and greater flexibility in selecting image plane position, orientation, and duration. Therefore, MRI-based 4D imaging technology is highly desirable in many clinical applications.

There are two main approaches to 4D image formation via MRI (Cai et al., 2011): (i) Using fast 3D MRI sequences to acquire real-time 3D volumetric data. (ii) Using fast 2D MRI sequences to continuously acquire 2D images from all respiratory phases, location by location spatially, then sifting these slices to select an optimal subset to form 4D images. For the real-time 3D approach, limited by current hardware and software, it is difficult to achieve high spatial resolution while ensuring adequate temporal resolution and image quality. Therefore, the 2nd retrospective approach has become the focus of current 4D MRI imaging research. In the past few decades, several approaches have been proposed to recover 4D information from the original 2D MRI sequences.

In the retrospective approach, 2D slices of a 3D volume are scanned separately during a number of breathing cycles. Slices from these 2D sequences are retrospectively stacked into 3D images (von Siebenthal et al., 2007). Since the 3D structure is not maintained in 2D MRI sequences, some form of internal or external respiratory surrogate is required to restore the respiratory motion, which is the most important part of these approaches. Consequently, these approaches inherit some drawbacks. External respiration devices, like respiratory belts, often have low correlation with the actual organ respiratory motion. Furthermore, external devices can affect the scanning process itself and are sometimes not suitable for patients with certain diseases (Remmert et al., 2007). Internal surrogates, like the 1D navigator echo in (von Siebenthal et al., 2007) and (Karani et al., 2019), can increase the scanning time and compromise the temporal resolution to some extent. To overcome these shortcomings, researchers have increasingly focused on extracting motion signals based only on the scanned image time series, which is often referred to as *self-gating* or *self-navigator* approach.

The basic idea of self-gating approaches is to derive motion signal from the image based on some features extracted from the image. Many methods have been proposed recently, which can be grouped into 3 main categories: feature-based surrogate, graph-based optimization, and manifold learning alignment.

Some studies use area of the body region in the MR images as an internal respiratory surrogate to extract the breathing signal (Cai et al., 2011; Liu et al., 2014; Yang et al., 2014). The success of such an approach depends on the accuracy of body region segmentation. Moreover, since only a portion of the body region is selected as a reference for the motion signal, these approaches require manual interaction for this selection which affects their efficiency and accuracy.

Tong et al. proposed a novel graph-based optimization approach (Tong et al., 2017), which formulates the 4D construction problem as an optimal path searching problem in a weighted graph where the acquired slices constitute vertices and arc weight is determined based on local spatial and temporal contiguity of slices. Based on this graph method, Romaguera et al. proposed a modified method that introduces the continuity of time into the graph weights to identify respiratory end phases automatically (Vázquez Romaguera et al., 2019). This method uses the vertical component median value of optical flow estimated around the diaphragm as a respiratory agent. Shortcomings of this method are that it does not consider chest wall motion, and a region of interest (ROI) is selected for the process based on some knowledge, which reduce its generality for some abnormal slices.

Manifold learning is another kind of self-gating approach for 4D MRI construction which embeds all acquired slices into one global low-dimensional space according to the respiration phase. Georg et al. used the Isomap technique with some alignment steps to determine respiratory phase from axial CT data (Georg et al., 2008). Wachinger et al. achieved gating with Laplacian Eigenmaps for both ultrasound and MR images, with a requirement that the lung region should be cropped first before manifold learning is performed (Wachinger et al., 2012). Baumgartner et al. proposed a novel method based on simultaneous group-wise embedding of data sets to increase the alignment robustness of manifold learning (Baumgartner et al., 2013). Clough et al. proposed an adapted version of Wave Kernel Signature (WKS) as the graph descriptor for Manifold Alignment where both image intensity and motion field are used to build the manifold (Clough et al., 2018). Additional manifold learning based methods for 4D MRI construction are demonstrated in (Baumgartner et al., 2015, 2014; Uh et al., 2016).

Methods focusing on radial k-space (Chen et al., 2017; Deng et al., 2016; Liu et al., 2015) have also been reported. Their major benefit is relative insensitivity to motion artifacts.

Although many of the above reviewed approaches provide an effective 4D MRI construction solution, they all share one or more of 3 key shortcomings. (i) They cannot handle the complex respiratory patterns associated with very sick, especially pediatric, patients whose data sets may contain several abnormal breathing cycles. (ii) They require some form of user input like an ROI or labels for end inspiration and end expiration phases (Tong et al., 2017), making them not completely automatic. This interferes with a production-mode operation where a large number of data sets are to be processed routinely. (iii) Most importantly, instead of scanning the complete thorax across the chest, it is often of interest to acquire dynamic data sets at selected spatial slice locations, for example, to cover just one or both of the hemi-diaphragms with just a few sparsely located slices. Some of the above methods run into difficulty because of their dependence on full data sets with closely positioned neighboring slices to recover 3D information, which are lacking in sparsely located slices.

In this paper, we present a fully automatic 4D dynamic MRI (dMRI) construction approach which by design tries to overcome the above hurdles. The approach centers around a novel concept we propose as a respiratory surrogate, called *optical flux*, and consists of three major steps. *Flux* is a physical quantity used to describe the properties of a region in a vector field, such as a magnetic field or an electric field. It represents the total "outgoingness" of the region with respect to the vectors in the region. In our set up, for each sagittal slice position through the thorax, a time series of slices is acquired and 4D construction is performed in three steps. Step 1 : For each sagittal position, we use an optical flow algorithm to estimate the motion vector field within the thoracic body region from successive slices in the time dimension. If a slice in the time series is in the inspiration phase, the vectors in the optical flow vector field will mostly point toward the body region boundary and the optical flux will be positive. Conversely, for a slice in the expiration phase, the flux will be negative. This step detects and outputs respiratory cycles via the mechanism of optical flux. Step 2 : In this step, abnormal cycles are detected and filtered out based on features extracted from the detected cycles. Step 3 : In this step, a 4D image is constructed representing the breathing 3D thorax over one respiratory cycle. For each sagittal position, one canonical cycle is created via a cosine model from the detected normal cycles. Subsequently, the cycles from the different sagittal positions are assembled together to form a 4D image.

We utilize dMRI data sets from 25 normal pediatric subjects and 58 pediatric patients with Thoracic Insufficiency Syndrome (TIS) as described in Section 2. Our complete flux-based 4D construction approach is described in Section 3. In Section 4, we present evaluation strategies and an analysis of the robustness of the key steps in the 4D construction method. In Section 5, we present the results and analyze them. In Section 6, we state our concluding remarks.

Materials

In this paper, we utilize dMRI data sets from 25 pediatric subjects with no known thoracic anomalies and 58 dMRI data sets from 29 patients with TIS where each patient had a dMRI scan before and after surgery. The scan data were obtained from the Children's Hospital of Philadelphia (CHOP) following approval from the Institutional Review Board at CHOP and the University of Pennsylvania along with a Health Insurance Portability and Accountability Act waiver. Each subject was scanned in the sagittal plane using the same imaging protocol from right lateral end to left lateral end under breathing conditions that are natural for the subject. There are several advantages of sagittal plane scanning for our application. (i) It allows us to capture slices during complete breathing cycles with minimal out-of-plane motion. (ii) The sagittal slice orientation requires a small field of view in the slice plane and therefore leads to fast 2D acquisition for the same spatial resolution (von Siebenthal et al., 2007). More importantly, it requires a fewer number of slices to cover the whole chest and specifically each hemi-thorax. (iii) The hemi-diaphragms, among the most important structures in our study, are digitized optimally relative to their 3D shape.

The dMRI scan protocol was as follows: 3T MRI scanner (Siemens Healthcare, Erlangen, Germany), true-fast imaging with steady-state precession sequence; TR/TE = 3.82/1.91 msec; voxel size, approximately $1 \times 1 \times 6$ mm^3; 320×320 matrix; bandwidth = 558 Hz; flip angle = 76°; and one signal average. For each of 30–40 sagittal plane locations through the thorax, slice data were obtained during 8–14 tidal breathing cycles at approximately 480 msec per slice amounting to about 80 time samples; total acquisition time per subject = 40 min. This process yields over 2000–3000 slices in total for one patient and constitutes a spatio-temporal sampling of the subject's dynamic thorax over 240–560 respiratory cycles.

The 83 dMRI scans employed in our study constitute a realistic mix of conditions that are commonly encountered in our application. Specifically, although the breathing rate was generally less rapid in normal subjects than in patients, surprisingly their scans more frequently contained abnormal breathing cycles due to shallow breathing or deep inhalation, etc., than the patient scans. In the TIS application, since our overall goal is to study thoracic dynamics under normal or tidal breathing conditions and the change in dynamics from pre- to post-operative condition (Tong et al., 2019), cycles constituting only tidal breathing among the data acquired over 240–560 cycles are relevant. Thus, our 4D construction method named OFx (symbolizing *Optical Flux*) should be able to automatically discard abnormal cycles in the acquired scan data. To give a preview of the data sets, we present a statistical portrayal of the length of the cycles for each of the 25 normal subjects and 58 patient scans in Fig. 1, where the subjects are sorted and arranged in the increasing order of their median cycle length from left to right. The continuous line represents the median length. For each subject, the lower and upper boundaries of the box represent the 25th and 75th percentiles of the respiratory period over all breathing cycles, and the upper and lower limits of the black line indicate the maximum and minimum lengths of tidal cycles that do not constitute outliers. The "+" mark represents outliers. As can be seen, the distribution of the cycle length is not uniform and there are many outliers. Some outliers with longer lengths represent cycles with deep breathing or cycles with a period of holding breath or very shallow breathing. Some outliers with shorter lengths may represent cycles with sharp and rapid breathing. Any robust 4D construction method should be able to cope with these outlier cycles automatically.

Methods

We propose a novel approach for 4D construction in this section. The goal of the 4D construction task is to recover the 4D information from uncoordinated spatio-temporal sampling of the 4D space via 2D slices. The most important requirement for this task is to preserve temporal and spatial continuity in the 4D constructed image. Temporal continuity is naturally obtained in the acquired data set but spatial continuity is broken due to the sampling process. Our construction method must restore the spatial continuity as much as possible under the premise of preserving temporal continuity. This is the most important strategy of our approach, which sets it apart from other methods. Another consideration is that if

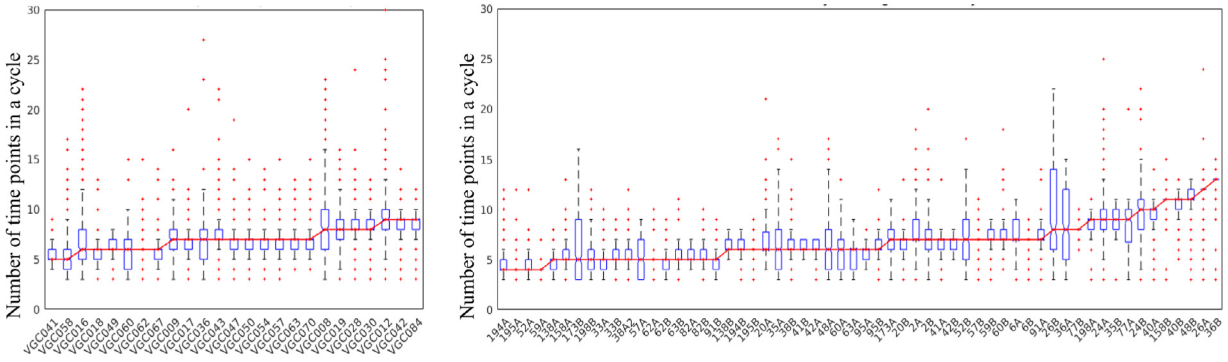

(a) (b)

Fig. 1. Cycle length statistics for (a) normal subjects and (b) TIS patients. The continuous curve depicts the median value for each subject; the box plot ends denote 25th and 75th percentile values. "+" denotes outliers.

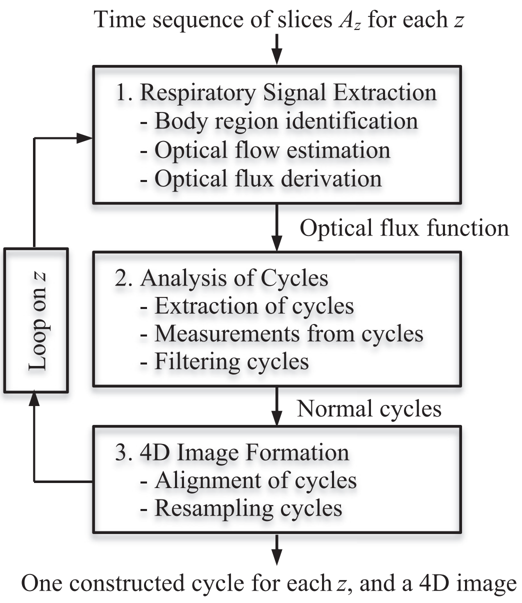

Fig. 2. The framework of the optical-flux-based 4D construction approach OFx.

the breathing cycles constructed from every sagittal location are normal and synchronized, then eventually the final constructed 4D image will have good spatial continuity. The strategy of the whole method can be summed up simply as follows: Each sagittal location proposes a constructed synchronous normal cycle independently, all of which together will constitute the final constructed 4D volume.

The overall 4D image construction approach, depicted schematically in Fig. 2, consists of three main steps: (i) Respiratory signal extraction; (ii) Cycle analysis; and (iii) 4D image formation. In the first step, we derive optical flux information, which can be regarded as a respiratory surrogate, from the time-series of slices associated with each sagittal location and extract all potential cycles. In the second step, we conduct a full analysis of these cycles at each location based on the flux data and extract all near-normal cycles. In the third step, we align all near-normal cycles to one canonical respiration model and propose one cycle for each location independently. These proposed cycles are finally combined from all locations to form the final 4D image volume. We will examine these steps in detail in the rest of this section.

3.1. Respiratory signal extraction

We assume that there is a time varying anatomic body region $B(t)$ (in our case, it is the entire region interior to the outer skin boundary) whose domain is contained in a rectangular region $\Omega = X \times Y \times Z$ mm^3. For each subject, Ω is defined and fixed by the imaging device *xyz* coordinate system. In practice, $X \times Y$ is the imaging field of view of the acquired 2D slices. Our dMRI free-breathing scanning method produces a sequence of slices$A = \{f_{z_1,t_1}, f_{z_1,t_2}, \ldots, f_{z_1,t_M}, f_{z_2,t_{M+1}}, \ldots, f_{z_2,t_{2M}}, \ldots, f_{z_N,t_{N\times M}}\}$ representing a spatio-temporal sampling of Ω over a total scanning time interval of $[0, \tau]$ within which 240–560 cycles are covered. Each slice f_{z_i,t_j} is acquired within a short time (~480 *ms*), when $B(t)$ can be assumed to be frozen in time/motion, such that $z_i \in Z$ and $t_j \in [0, \tau]$. Note that in our protocol the *z*-axis is orthogonal to the sagittal plane, typically N (the number of sagittal or *z* locations) is 30 to 40, meaning that slices are acquired for N sagittal slice locations, and the number of time points M for each sagittal location is usually 80. The $+y$ direction is caudo-cranial, $+x$ direction is postero-anterior, and the $+z$ direction is right to left. For convenience, we will denote the sequence of slices associated with a specific *z*-location by $A_z = \{f_{T_1}, f_{T_2}, \ldots, f_{T_M}\}$, $z = z_1, z_2, \ldots, z_N$, and $T_1, \ldots, T_M$ denote the time instances associated with the slices in A_z. Since there is no time coordination among slices in A, it constitutes an uncoordinated spatio-temporal sampling of Ω over the time interval $[0, \tau]$. In other words, the respiratory phases of the slices in the two time sequences A_{z_i} and A_{z_j} associated with any two distinct *z*-locations z_i and z_j are not synchronized. Our approach actually constructs one cycle for each *z*-location such that the constructed cycles for any z_i and z_j are in synchrony.

In this step of the approach, processing of the time series A_z is done independently for each z to output a respiratory signal depicting all potential cycles in each A_z. There are three sub-steps employed in this part: body region identification, optical flow estimation, and optical flux derivation, as described below.

3.1.1. Body region identification

Our goal is to infer the pseudo-periodic motion of the tissues due to respiration within the body region $B(t)$ from the sequence of slices A_z at each specific *z*-location. To avoid background noise outside the body region in the images influencing the estimation of flux, we first roughly segment the body region in the given image sequence A_z, as illustrated in Fig. 3. For the body region in a slice f_{T_i} of A_z as shown in Fig. 3(a), we will denote the segmented body region by R_i as illustrated in Fig. 3(c). All subsequent operations will be confined to the segmented body region R_i.

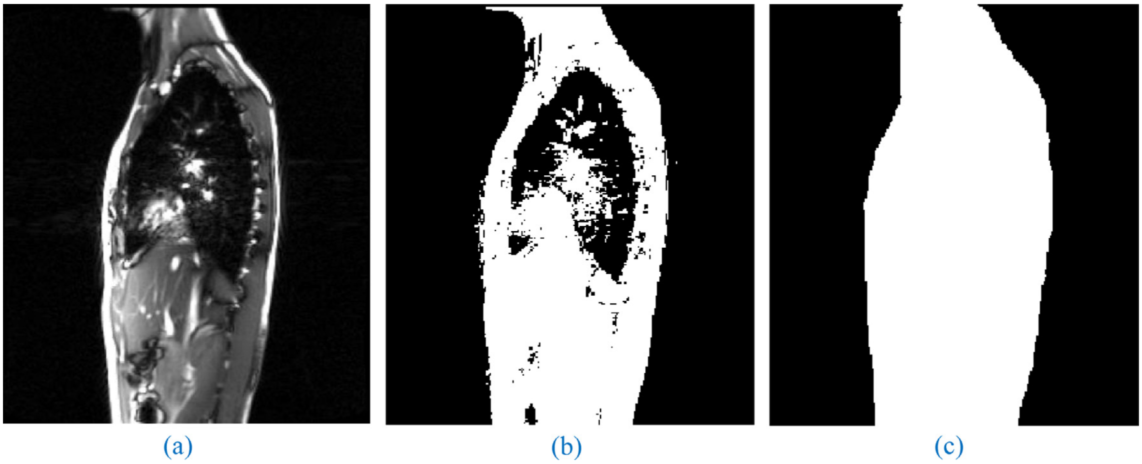

Fig. 3. Illustration of body region segmentation via thresholding. (a) An original MRI slice from A_z. (b) Binary image after thresholding the image in (a). Binary image after opening followed by closing operations.

It is rather straightforward to segment the body region via thresholding followed by morphological opening and closing operations. The binary image after thresholding the image in Fig. 3(a) is shown in Fig. 3(b), and the final segmented result is shown in Fig. 3(c). We can see that the body region has been segmented very well. We emphasize that precise segmentation of the body region is neither the goal nor a necessary requirement since minor inaccuracies will not influence flux estimation. We estimate threshold $\theta 1$ experimentally and fix it at 1000. We use a structuring element consisting of the 4 edge-adjacent neighbors for one opening operation followed by a 24-neighbor (within the 5 × 5 neighborhood) structuring element for one closing operation. We have examined the body region segmentation results for all data sets used in this paper and confirmed that the method works very robustly in the above sense.

In Section 4.1, we will demonstrate that optical flux estimated for region R_i is largely not influenced by the size or shape of R_i.

3.1.2. Optical flow estimation

The mechanism of optical flow assumes that the motion under consideration at every pixel (x, y) is small in going from slice $f_{T_{i-1}}$ at $T_{i\text{-}1}$ to slice f_{T_i} at T_i. This leads to the image constraint equation shown below where $\Delta t = T_i - T_{i\text{-}1}$ and $(x+\Delta x,\ y+\Delta y)$ denotes a pixel neighboring pixel (x, y).

$$f_{T_i}(x+\Delta x, y+\Delta y) = f_{T_{i-1}}(x, y). \tag{1}$$

With the assumption of small motion from $T_{i\text{-}1}$ to T_i, by Taylor series expansion,

$$f_{T_i}(x+\Delta x, y+\Delta y) = f_{T_{i-1}}(x, y) + \frac{\partial f_{T_i}}{\partial x}\Delta x + \frac{\partial f_{T_i}}{\partial y}\Delta y + \frac{\partial f_{T_i}}{\partial t}\Delta t + \varepsilon, \tag{2}$$

where ε denotes residual sum over higher order terms in the series. If we divide throughout by Δt, the $\varepsilon/\Delta t$ will tend to 0 when Δt tends to 0 and the above equation leads to

$$\frac{\partial f_{T_i}}{\partial x}u + \frac{\partial f_{T_i}}{\partial y}v + \frac{\partial f_{T_i}}{\partial t} = 0, \tag{3}$$

where $(u, v)^t = (\frac{\Delta x}{\Delta t}, \frac{\Delta y}{\Delta t})^t$ denotes the velocity vector with its horizontal (antero-posterior) component u and cranio-caudal component v at pixel $p = (x, y)$ at time $t = T_i$. We employ the Lucas–Kanade method (Lucas and Kanade, 1981) to solve for u and v based on the assumption that the optical velocities in local neighborhoods of each pixel $p = (x, y)$ are similar.

$$\begin{bmatrix} u \\ v \end{bmatrix} = \begin{bmatrix} \sum\limits_{(x,y)\in L(p)} \frac{\partial^2 f_t(x,y)}{\partial x^2} & \sum\limits_{(x,y)\in L(p)} \left(\frac{\partial f_t(x,y)}{\partial x}\right)\left(\frac{\partial f_t(x,y)}{\partial y}\right) \\ \sum\limits_{(x,y)\in L(p)} \left(\frac{\partial f_t(x,y)}{\partial x}\right)\left(\frac{\partial f_t(x,y)}{\partial y}\right) & \sum\limits_{(x,y)\in L(p)} \frac{\partial^2 f_t(x,y)}{\partial y^2} \end{bmatrix}^{-1} \begin{bmatrix} -\sum\limits_{(x,y)\in L(p)} \left(\frac{\partial f_t(x,y)}{\partial x}\right)\left(\frac{\partial f_t(x,y)}{\partial t}\right) \\ -\sum\limits_{(x,y)\in L(p)} \left(\frac{\partial f_t(x,y)}{\partial x}\right)\left(\frac{\partial f_t(x,y)}{\partial t}\right) \end{bmatrix}. \tag{4}$$

The mechanism of optical flow generates a *vector field* $V_i(p)$: $R_i \rightarrow \mathrm{R}^2$, which is a mapping from the discrete body region R_i in 2D image plane to the vectors in the 2D space R^2 corresponding to time instance T_i. In other words, to every pixel $p = (x, y)$ in R_i identified in slice f_{T_i}, we assign a vector $(u, v)^{\mathrm{t}}$ which indicates the velocity vector at p at time T_i.

Since we estimate optical flow based on the identified discrete body region R_i, the OFx process reduces the impact of background noise from outside the body region influencing analysis within the body region. This idea is crucial for capturing the motion of lungs and hemi-diaphragms precisely. Two examples of optical flow estimated within the body region R_i are shown in Fig. 4. In Fig. 4(a), the two time-adjacent slices are in the inspiration phase. The optical flow vector field in this case generally points outwards the body region boundary. In Fig. 4(b), the two time-adjacent slices are in the expiration phase, and the vector field points inwards as shown. From a close scrutiny of all data sets, we observed that optical flow can capture the non-rigid local movement within the body region precisely and robustly. This robust means of estimating optical flow led us naturally to formulate optical flux as a respiratory surrogate.

3.1.3. Optical flux of body region

Flux is a property associated with a region in a vector field introduced by Maxwell (Maxwell, 1881). It represents the net "outgoingness" for that region. One typical application of flux is in electric fields. For a dipole (a pair of electric charges of equal magnitude but opposite sign separated by a small distance), the electrostatic potential field it generates is typically as shown in Fig. 5. As we can see, the flux (net outgoingness) of any region like A (including the +ve charge) will be positive, the flux of a region like B (including a -ve charge) will be negative, whereas the flux of a region like C (without containing any charges) will be zero. For region D, which includes both +ve and -ve charges, the flux going into and out of D are the same and hence its net outgoingness will be 0.

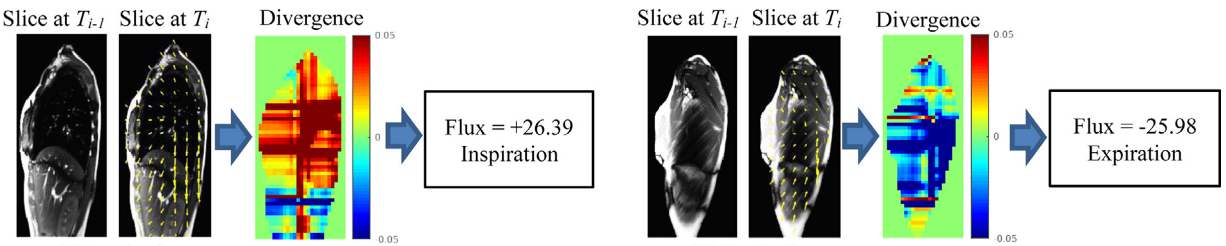

(a) Inspiration (b) Expiration

Fig. 4. Examples of optical flow and flux within the body region in (a) inspiration and (b) expiration illustrated for two consecutive slices in a time sequence A_z.

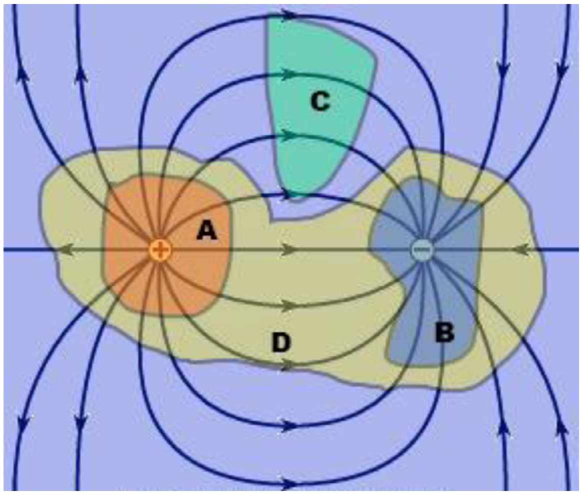

Fig. 5. Illustration of the concept of flux. Flux for the three depicted regions A, B, and C are positive, negative, and 0, respectively. Flux for region D, which includes both A and B, is also 0.

In our case, we have the vector field $V_i(p)$ generated by the mechanism of optical flow to capture the motion of the tissues within the body region R_i as explained above and depicted in Fig. 4. Although the notion of flux is applicable to any region within the slice domain, our focus will be the segmented body region R_i. During inspiration, chest wall and diaphragm move outward with respect to the lung tissues, which is reflected in the outward direction of the vectors in $V_i(p)$ as shown in Fig. 4(a). (From the electric field analogy, this situation is as if there is positive electric charge inside the body region and negative charge outside.) Toward the end of inspiration, this outgoingness will gradually decrease and reverse during inspiration when the vectors will change direction to orient generally inwards corresponding to the inward motion of the chest wall and diaphragm, as in Fig. 4(b). (Analogously, the interior positive charge gets gradually depleted toward the end of inspiration, with a reversal of charge to negative inside and positive outside during exhalation.)

The method to derive flux from the vector field is through the concept of *divergence*, $div(V_i)$, (or derivative) of the vector field $V_i(p)$. Divergence (Korn and Korn, 2000) at a point (pixel) p in *Vi* is a local measure of outgoingness at p. In other words, it denotes the amount (a scalar) of outward flux locally within an infinitesimal volume (area) around p.

$$div(V_i) = \nabla \cdot V_i = \left(\frac{\partial}{\partial x}, \frac{\partial}{\partial y}\right)^t \cdot (u, v)^t = \frac{\partial u}{\partial x} + \frac{\partial v}{\partial y} \tag{5}$$

The divergence map (divergence value at each pixel) for the optical flow vector field is shown in the Divergence part of Fig. 4. Notably, the divergence at most pixels in Fig. 4(a) is positive, as indicated by the red end of the color scale. On the other hand, the divergence at most pixels in Fig. 4(b) is negative, as depicted by the blue end of the color scale. The total outgoingness for body region R_i corresponding to time point T_i (and slice location z), which we will term *optical flux* $\Phi_z(T_i)$, is simply an integral of divergence over R_i.

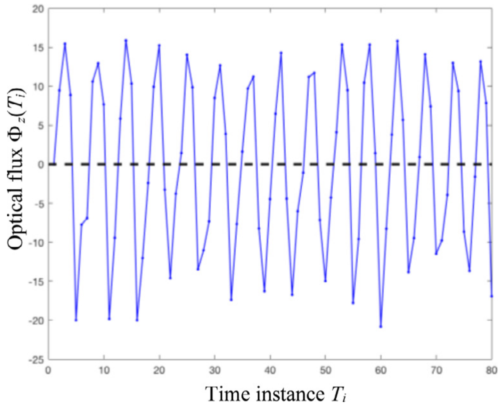

Fig. 6. Optical-flux curve $\Phi_z(T_i)$ derived from the dMRI scan A_z of a normal pediatric subject for one z location.

$$\Phi_z(T_i) = \sum\nolimits_{p \in R_i} div(V_i(p)). \tag{6}$$

As we can see, the optical flux for the inspiration phase depicted in Fig. 4(a) is positive and that for the expiration phase in Fig. 4(b) is negative[1].

After estimating optical flux for each time point T_i in A_z based on adjacent time slices in A_z as expressed by Equations (1)–(6), we derive an optical-flux curve $\Phi_z(T_i)$ associated with A_z as shown in Fig. 6, which can be regarded as a surrogate to respiratory signal associated with sagittal slice location z. Notably, optical flux can represent the respiratory signal remarkably accurately!

From the definition of flux, we can see that it is an indicator to measure the total "outgoingness" of a certain region in the vector field. For the optical flow field, flux can represent the total amount of movement outwards or inwards with respect to the region. In this case, movement is mainly caused by air entering or leaving the body. The magnitude of movement is highly correlated with the amount of breathing. Therefore, from another perspective, the optical flux can be also regarded as the air flux entering or leaving the human body. In summary, the body region R_i as the reference region for estimating flux is simple and effective. In Section 4.1, we will examine if and how the size of the body region may affect $\Phi_z(T_i)$.

---

[1] The unit of measurement for flux is mm/second. The values shown in Fig. 4 are in mm per unit time slice. Since our time slices are roughly 480 msec apart, these flux values should be divided by 480 to express them in physical units.

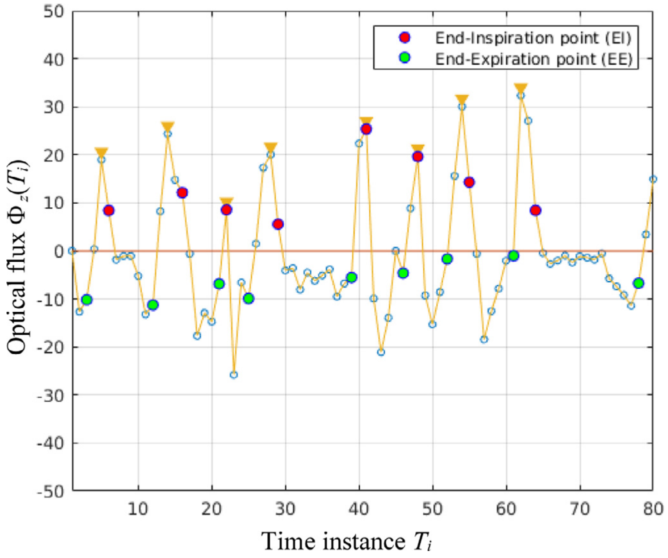

Fig. 7. EI and EE points detected on the flux curve $\Phi_z(T_i)$ derived from the dMRI scan A_z of a TIS patient.

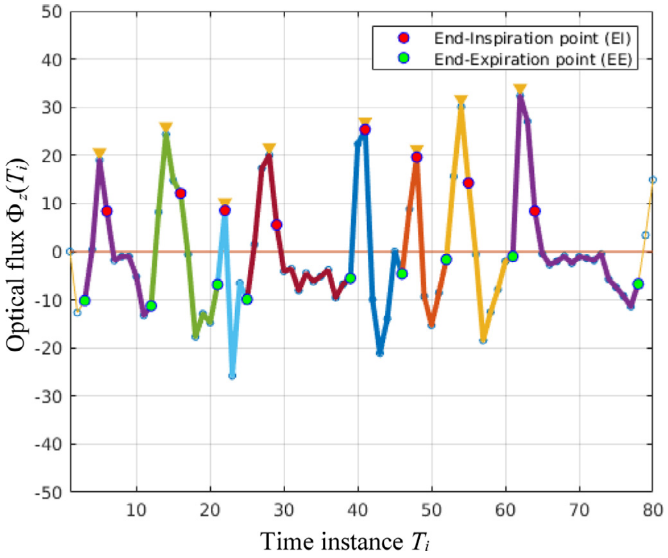

Fig. 8. Cycles detected on the flux curve $\Phi_z(T_i)$ derived from the dMRI scan A_z of a TIS patient.

3.2. Analysis of Cycles

Typically, A_z includes 10–15 cycles in the $\Phi_z(T_i)$ curve associated with A_z. Some of these cycles are near-normal, constituting tidal breathing, and others are abnormal, representing shallow or deep breaths, etc. In this step, for each time sequence A_z corresponding to each z location, the goal is to output the set of "normal" cycles contained in $\Phi_z(T_i)$, denoted $\mathrm{C}_z = \{\mathrm{c}_1, \ldots, \mathrm{c}_m\}$, and the associated set of subsequences of time slices in A_z, denoted $\mathrm{S}_z = \{\mathrm{s}_1, \ldots, \mathrm{s}_m\}$. Toward this end, we (i) first identify the End-Inspiration (EI) and End-Expiration (EE) time points (Fig. 7) in $\Phi_z(T_i)$ and identify all cycles in $\Phi_z(T_i)$; (ii) derive features from cycles to help classifying them as normal or abnormal; and (iii) classify cycles, based on features, and filter out abnormal cycles to output C_z and S_z. These individual steps are described below.

3.2.1. Extraction of cycles

The goal of this step is to identify EI and EE time points in $\Phi_z(T_i)$ and thereby partition $\Phi_z(T_i)$ into respiratory cycles. If all respiratory cycles are near-normal as in the example in Fig. 6, we can detect EI and EE points easily depending on the zero-crossings of the flux curve. However, A_z typically contains abnormal patterns. An example is illustrated in Fig. 7. Notably there are shallow-breathing or breath-holding patterns with $\Phi_z(T_i)$ hovering around 0. After examining images manually, we found that the reason for the flux curve appearing irregular was not due to any deficiencies with the concept of flux or its estimation, but was instead due to the real breathing motion pattern, where the flux curve *truly portrays it*.

To detect EI and EE points, we first find all peaks on the $\Phi_z(T_i)$ curve and then filter out peaks with values close to 0. The final detected peaks are shown in Fig. 7, represented by triangles. Then, following the time sequence, we find the last time point (slice) with positive flux after each peak as an EI point and the first slice with negative flux before each peak as an EE point. The detected EI-EE points are displayed in Fig. 7.

With the detected EI-EE points, we can extract all cycles in A_z by just following the EI-EE sequence and simply taking the subsequence of time points from one EE point to the next EE point in the sequence as one cycle, as shown in Fig. 8.

3.2.2. Deriving features from cycles

In natural breathing, the patterns of movement are quite varied and complex. After closely studying these patterns from 1000 s of cycles in our data set, we arrived at 4 major rules that characterize respiratory movement as described below. These rules guide us to define the features that will be used to distinguish between normal and abnormal cycles.

1) *Rule* 1: The tidal volume is the most important feature to distinguish between normal and abnormal cycles. Typically, there are 8–14 cycles in one acquired sequence of slices (A_z). Normal cycles always have a stable tidal volume but abnormal cycles do not. For example, tidal volume of deep breathing cycles will be much greater and that of shallow breathing cycles will be much smaller. Reflected in the signal, the tidal volume for a sagittal location over a cycle is the sum of the optical-flux of all time points in the cycle. This rule alone can distinguish most abnormal cycles in the signal from normal cycles, but to make the analysis more detailed so border-line cycles are also detected, we have included additional rules.
2) *Rule* 2: In very few breathing cycles, hesitation seems to appear during tidal movement. For example, when breathing moves towards inspiration, the breathing pauses suddenly and a slight exhalation takes place (it is too short to be considered a cycle), but then quickly returns to the inspiration process. Reflected in the breathing signal, this will show one or more peak(s) or valley(s). The impact of this kind of cycles on construction is low and very few such cases exist.
3) *Rule* 3: The relationship between the inspiratory tidal volume and the expiratory tidal volume can also be regarded as a feature that distinguishes abnormal cycles. Their ratio in the normal cycle should be ~1, but the ratio in the abnormal cycle will be much smaller or much larger. When we evaluate absolute tidal volume, Rule 1 already covers this situation to some extent. Here we use it as an additional rule to make our analysis more refined and robust.
4) *Rule* 4: Some cycles may have an abrupt stop at the end of inspiration. Some cycles may stay for a while at the endpoint. Although these cycles can be considered normal cycles (if their volumes in *Rule* 1 are acceptable), we can use this rule to determine which cycle is more normal. This phenomenon is re-

flected in the signal as the time distance from the peak to the endpoint.

To implement these rules (*Rule* 1-*Rule* 4), we derive the following features from each cycle identified in $\Phi_z(T_i)$.

Flux volume during inspiration ($F1$) *and expiration* ($F2$): $F1$ is defined as the sum of the fluxes $\Phi_z(T_i)$ associated with the time points T_i corresponding to the inspiration phase of the cycle. $F2$ is similarly defined for the expiration phase of the cycle but by taking only the magnitude and ignoring the sign. $[F1 + F2]$ represents the total flux for the cycle.

Number of peaks ($F3$) *and valleys* ($F4$): These features express the degree of smoothness of the respiratory motion of the cycle. Since the instantaneous flux $\Phi_z(T_i)$ represents the speed of motion of the body region R_i at time T_i, the smaller $F3$ and $F4$ are, the smoother will be the motion of R_i within the cycle. Ideally, we should have one peak and one valley in a cycle. In the example displayed in Fig. 8, the first cycle has 2 peaks and 2 valleys, the 3rd cycle has 1 peak and 1 valley, and the 4th cycle has 3 peaks and 3 valleys.

Time distance between peak and EI time points ($F5$): It also represents the smoothness of the movement in the cycle. It denotes the time taken from the fastest positive speed to change to a negative speed. In Fig. 8, the distance is 2 for the 2nd cycle and 0 for the 3rd cycle.

3.2.3. Filtering cycles

We design four loss functions L_1-L_4 corresponding respectively to the 4 rules as explained below. First, according to the characteristics of each rule, we choose a parametric function such as linear, hyperbolic, exponential, etc. Second, we solve for the parameters of the functions based on the rules.

1) L_1: This loss function follows *Rule* 1. First, we define Fm as the median of cycle volumes $[F1 + F2]$ over all cycles in the signal associated with each z location. Then variable x is defined as the ratio $x = (F1 + F2 - Fm)/Fm$. The greater this ratio, the deeper the breathing is in this cycle. The smaller the ratio, the shallower is the breathing. The best case is when the ratio is zero. The loss should increase exponentially as the ratio increases in the positive direction and increase exponentially with a negative exponent as the ratio becomes more negative. Therefore, we define $L_1(x)$ via an exponential model as follows:

$$L_1(x) = \left|7^{x+P1} + P2\right|, \tag{7}$$

where $P1$ and $P2$ are the model parameters. Clearly, when $x = 0$, $L_1 = 0$. We normalize the loss range to [0, 1]. We also define the tolerable boundary based on experience. When $x = 0.7$, we would like L_1 to be 1. This means $x = 0.7$ is the acceptable boundary of the normal breathing cycle, which is normalized to 1. The reason for using 7 as the base is that we wish to adjust the ratio of the positive (deep breathing) and negative (shallow breathing) parts of the function[2]. Shallow breathing has little effect on the subsequent construction process, which should be assigned a smaller loss. Thus, our conditions are

$$\begin{cases} x = 0 \Rightarrow L_1(x) = 0 \\ x = 0.7 \Rightarrow L_1(x) = 1. \end{cases} \tag{8}$$

After substituting these 2 cases into the function model, we can solve for parameters P1 and P2, which come out to be -0.5479 and -0.3443, respectively. The final form of L_1, as depicted in Fig. 9(a) will be:

$$L_1(x) = \left|7^{x-0.5479} - 0.3443\right|. \tag{9}$$

2) L_2: This loss function follows *Rule* 2. The number of peaks and valleys is $x = [F3 + F4]$. Based on our cycle extraction process, $x \geq 2$. As x increases, L_2 should also increase exponentially. However, x cannot grow indefinitely. When x approaches a certain value, we would want $L_2 \to +\infty$. So, the model for L_2 can be chosen to be:

$$L_2(x) = \frac{P3}{x + P4} + P5, \tag{10}$$

where $P3$, $P4$, and $P5$ are the parameters of the model. When $x = 2, L_2$ should be 0. As $x \to 30$, we would like $L_2 \to +\infty$. Considering the number of time points in a cycle, $x = 30$ is large enough where $L_2(x)$ should approach $+\infty$. As with L_1, we define the tolerable boundary to normalize the loss to [0, 1]. When $x = 4, L_2 = 1$. Because the normal respiratory cycle contains only one peak and one valley; 4 is the tolerable boundary for normal cycles. Thus, our conditions are

$$\begin{cases} x = 2 \Rightarrow L_2(x) = 0 \\ x = 30 \Rightarrow L_2(x) = +\infty \\ x = 4 \Rightarrow L_2(x) = 1. \end{cases} \tag{11}$$

After substituting these 3 cases into the function model, we can solve for $P3$, $P4$, and $P5$, which yields $P3 = -364, P4 = -30$, and $P5$ = -13. The final definition of L_2, as depicted in Fig. 9(b), will be

$$L_2(x) = \frac{364}{30 - x} - 13. \tag{12}$$

3) L_3: This loss function follows *Rule* 3. Here we define $x = |F1 - F2|/(F1 + F2)$ and L_3 to exponentially increase with x. But unlike L_1, x cannot be too large since lung vital capacity is limited. Therefore, we formulate L_3 as an inverse function of x as

$$L_3(x) = \frac{P6}{x + P7} + P8, \tag{13}$$

where $P6$, $P7$, and $P8$ are parameters of the model. When $x = 0$, L_3 should be 0. Also, as $x \to 1$ we would like $L_3 \to +\infty$. For the tolerable boundary, when $x = 0.2, L_3 = 1$. In normal cycles, inspiration and expiration volumes should be almost the same, 0.2 is the tolerable ratio for normal cycles. Thus, our conditions are

$$\begin{cases} x = 0 \Rightarrow L_3(x) = 0 \\ x = 1 \Rightarrow L_3(x) = +\infty \\ x = 0.2 \Rightarrow L_3(x) = 1. \end{cases} \tag{14}$$

After substituting these cases into the model, we arrive at $P6$ = -4, $P7$ = -1, and $P8$ = -4. The final model of L_3, as depicted in Fig. 9(c), will be

$$L_3(x) = \frac{4}{1 - x} - 4. \tag{15}$$

4) L_4: The design of this loss function follows *Rule* 4. By examining all cycles, we found that $F5$ for most normal cycles is in the range 0–3, with $F5 = 1$ and 2 being the best. To formulate $L4$, we define $x = F5$. We would like $L_4(x)$ to increase faster than linearly with x and so define our model as a quadratic function, with the symmetric point situated at $x = 1.5$, as

$$L_4(x) = \frac{(x + P9)^2 + P10}{P11}, \tag{16}$$

---

[2] We found that when employing the commonly-used 2 as the base, the value of L_1 is not much different when x is positive vs. when x is negative; for example, when $x = 0.7$, $L_1(x) = 1$, and when $x = -1$, $L_1(x) = 0.8$. But in fact, in the subsequent reconstruction process, shallow breathing has little effect on the quality of the final reconstruction result, while deep breathing does. Therefore, we need to adjust the Loss values when x is negative to smaller values. Therefore, while keeping other conditions unchanged, we compared among the bases 2, 5, 7, and 10 and observed that in the four functions, the curve does not change much when x is positive. However, the part where x is negative changes more drastically. From 2 to 5, the loss value when $x = -1$ changes greatly, but from 5 to 7 and then to 10, the loss value when $x = -1$ changes very little. Thus, we empirically choose 7 as the base.

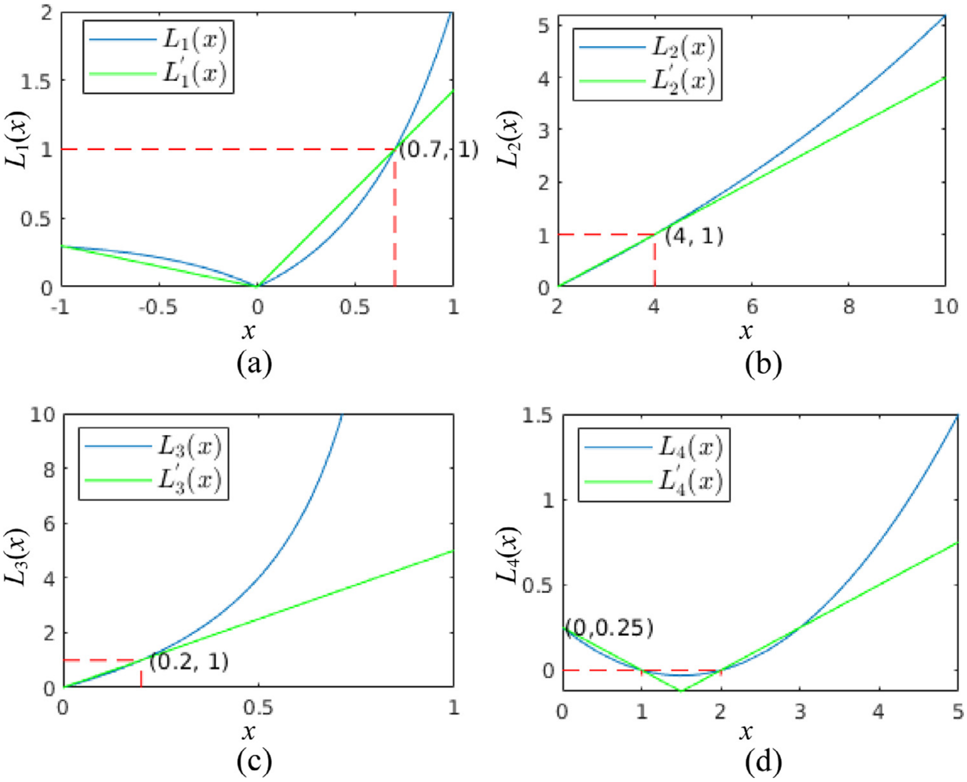

(a) (b) (c) (d)

Fig. 9. Loss functions L_1-L_4 employed in filtering cycles. Variable x denotes the feature combinations used in the definition of each loss function. Their counterpart linear formulations $L_1' - L_4'$ described in Section 4.2.1are also shown.

with $P9$, $P10$, and $P11$ as model parameters. For $x = 1$ and 2, L_4 should be 0, and when $x = 0$, we would like $L_4 = 0.25$. The tolerable boundary of L_4 will be between 4 and 5 as shown in Fig. 9(d). Thus, our conditions are

$$\begin{cases} x = 1 \Rightarrow L_4(x) = 0 \\ x = 2 \Rightarrow L_4(x) = 0 \\ x = 0 \Rightarrow L_4(x) = 0.25. \end{cases} \tag{17}$$

Again, solving for the parameters, we get $P9$ = -1.5, $P10$ = -0.25, and $P11$ = 8. The final model of L_4, as depicted in Fig. 9(d), will be

$$L_4(x) = \frac{(x - 1.5)^2 - 0.25}{8}. \tag{18}$$

Since we have normalized the losses to [0, 1], 0 is the ideal value for each loss function $L_i(c)$ associated with each cycle c and 1 is the normalized tolerable boundary value. We combine them linearly as in Eq. (19) such that $w_1 + \ldots + w_4 = 1$.

$$L(c) = \sum_{i=1}^{4} w_i L_i(c) \tag{19}$$

From the goal of cycle analysis, *Rule* 1 is the most important rule, the remaining being auxiliary ones. So, we set $w_1 = 0.7$ and the others such that they sum up to 0.3. The composite loss function $L(c)$ assigns a score to each cycle c in [0, 1], 0 being the best score and 1 being at the tolerable boundary for normal cycles. We set a threshold $\theta 2$ such that if $L(c) \geq \theta 2$, then c is considered to be abnormal. Due to the complexity of human breathing, 1 is just a fuzzy boundary. Therefore, we should set $\theta 2$ between 0 and 1. We fix $\theta 2$ at 0.4 experimentally since we observed that $L(c)$ of most abnormal cycles is greater than 0.4. A special case needs attention, for a z location where there is no cycle with $L(c)$ less than 0.4, we select the cycle with the smallest loss as the normal cycle. Some examples of cycles detected from a flux curve together with their $L(c)$ values and the normal cycles resulting after filtering are displayed in Fig. 10. The figure suggests that the filtering method is effective in weeding out cycles that are clearly abnormal.

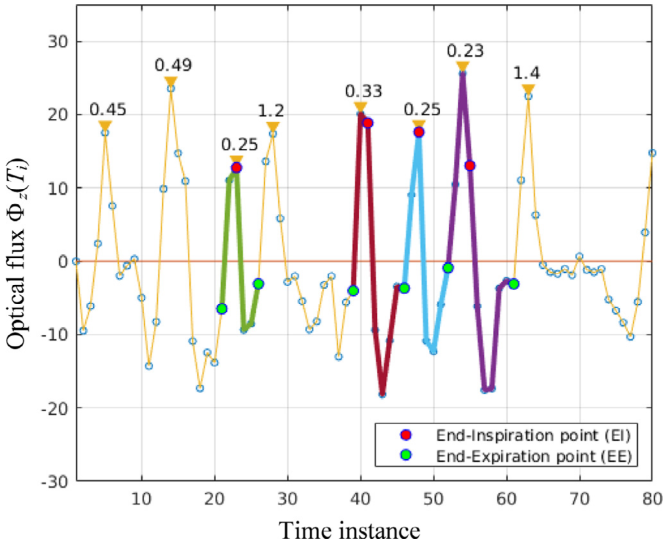

Fig. 10. An example of cycles for a flux curve $\Phi_z(T_i)$ derived from the dMRI scan A_z of a TIS patient together with the associated loss value of each cycle. The selected "normal" cycles after filtering are shown in bold.

3.3. 4D Image Formation

The final output from the previous step is set C_z of normal cycles contained in $\Phi_z(T_i)$ for each z-location and the associated set S_z of image sequences. Note that C_z is determined for each z independently of other z-locations. This stance is intentional and makes

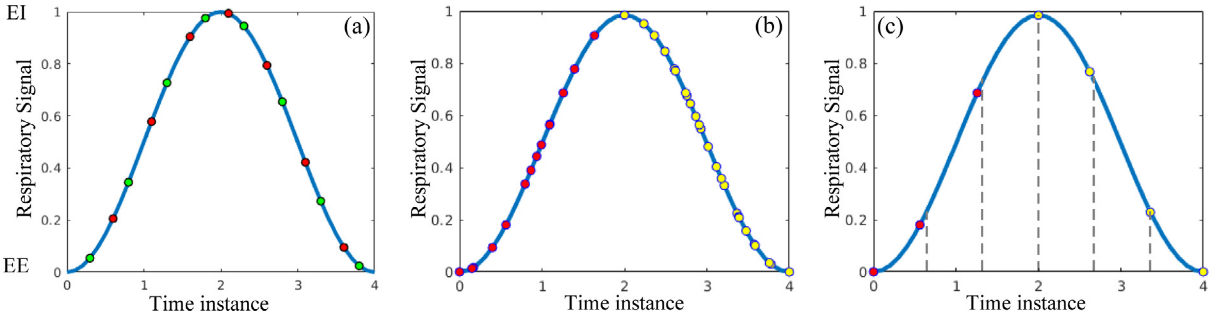

Fig. 11. (a) Cosine model for normal respiratory cycle. Time instances from two different normal cycles (red and green) are mapped on to the model. The x-axis represents respiratory phase and the y-axis denotes the flux volume as a surrogate for the position of the diaphragm. (b) Time instances from all m normal cycles from a z-position are mapped on to the model where the inspiration (red) and expiration (yellow) phases are shown in different colors. (c) A model cycle with equi-spaced time instances marked by dashed lines for $m_c = 7$, and the actual time instances selected (marked in red/ yellow) from the composite normal cycle c_{zn} in (b).

OFx general and, as we explain in Section 4, capable of handling situations where we may wish to acquire dMRI time sequences for very few z-locations and still be able to perform 4D construction and analysis. However, it has so far completely ignored the spatial contiguity in the z dimension. The purpose of this step is exactly to handle this factor to finally form a 4D space-time image. This goal is accomplished in three steps: (i) Modeling respiratory cycle. (ii) Constructing one composite respiratory cycle c_{zn} per z-location guided by the model based on all cycles in C_z. (iii) Resampling cycles c_{zn} for different z-locations to form the 4D image.

3.3.1. Modeling respiratory cycle

The ventilation model of human respiration has been studied in the past (Crooke et al., 2002; Low et al., 2005; Mols et al., 1999; Quanjer et al., 1993). Seemingly, a trigonometric function (like cosine) can accurately model this phenomenon, even though normally there is a slight difference between the lengths of the inspiration and expiration phases. As such, some 4D construction methods have employed a trigonometric function with only one parameter as an approximation of the respiration model (Clough et al., 2018; Uh et al., 2016). There are several reasons in support of this approximation. First, typically the acquisition temporal sampling frequency is not large enough to capture the details of this asymmetry, since only about 5–7 time points are sampled in one respiratory cycle. Second, for the subsequent analysis of the constructed 4D image for tidal volume estimation, it is more important to capture the slices at the EI and EE points than at other time points. So, we adopt a cosine function as shown in Fig. 11 as the model.

Now, consider two different cycles c_i and c_j in set C_z. Since slices are acquired under free breathing conditions, the number of and the actual respiratory phases of sampled time points in c_i and c_j will be generally quite different. However, once we perform a cosine fit to c_i and c_j, each separately, we will know within the fit cosine model, the exact phase of each time instance in the two cycles. This idea is illustrated in Fig. 11(a) where time instances from two cycles are mapped on to a single cosine model. Note that the basis for this idea is the use of flux as a surrogate for respiratory function. The flux value for each time slice can be regarded as the moving velocity of the slice. For each cycle c in C_z, we can estimate the moved distance from velocity for each time slice in c by accumulation, which can be regarded as the tidal volume signal of the slice in the cycle. For all cycles in C_z, we normalize the position signal from [min value, max value] to [-1, 1]. Following this procedure, we can align all time slices of the cycles in C_z into the cosine model as presented in Fig. 11(b).

3.3.2. Constructing one composite cycle c_{zn} per z-location

To construct one normal cycle for each z-position, we simply follow the above principle of mapping time instances from all cycles in C_z to the same model. This results in a single cycle c_{zn} and the associated time sequence s_{zn} of slices, which is a subset of the slices in A_z. This process is illustrated in Fig. 11(b). Note that the model facilitates aligning all cycles for z.[3]

3.3.3. Resampling cycles c_{zn} for different z-locations

Given c_{zn} and the associated time sequence of slices s_{zn}, for $z = z_1, \ldots, z_N$, in this step, we first obtain the minimum number m_c of time samples in the composite cycles c_{zn} over all z. Subsequently, from each cycle c_{zn}, we select m_c time samples as maximally uniformly distributed over the cycles as possible. In other words, we first divide the model cycle into m_c equal instances and mark these time instances. The actual time instances for which data were acquired that are closest to these marked ideal instances are then selected from c_{zn}. This process is illustrated in Fig. 11(c) for the case of $m_c = 7$. This process yields a cycle c_{zns} and the associated time sequence of slices s_{zns} for each z. Finally, the 4D constructed image corresponding to the acquired data set A is obtained by simply compiling together the slices in the sequences s_{zns} over all z.

OFx has an interesting and desirable theoretical property: Let A_1 and A_2 be two dMRI acquisitions such that the z-locations for A_2 are a subset of the z-locations for A_1 and the corresponding constructed 4D images be I_1 and I_2, respectively. Then I_2 will be a proper sub-image of I_1 in the sense that the slices in I_2 will be a subset of the slices in I_1.

OFx as a process as a whole has only two key parameters: Threshold $\theta 1$ used for body region identification and threshold $\theta 2$ on the loss function L(c). The process for estimating these parametric values has already been described in this section.

Method Analysis

In this section, we will first outline our evaluation strategies and metrics and then analyze the robustness of two key steps in the whole methodology: (a) body region identification (Section 3.1.1) and (b) filtering cycles (Section 3.2.3). We employ five metrics as follows. Metrics (i) and (ii) are used for robustness analysis, and metrics (ii)-(v) are used to evaluate the accuracy of the 4D construction process from different perspectives, with (ii) and (iii) referring to the temporal aspect and (iv) and (v) to the spatial component. Experiments and results for the actual performance evaluation of the method is presented in the next section.

---

[3] Possibly, the detected EE and EI points can also be used to measure phase within each cycle by assuming that phase changes linearly from EE to EI and EI to EE. The accuracy of this method will depend on hitting the EE and EI time points accurately while acquiring data.

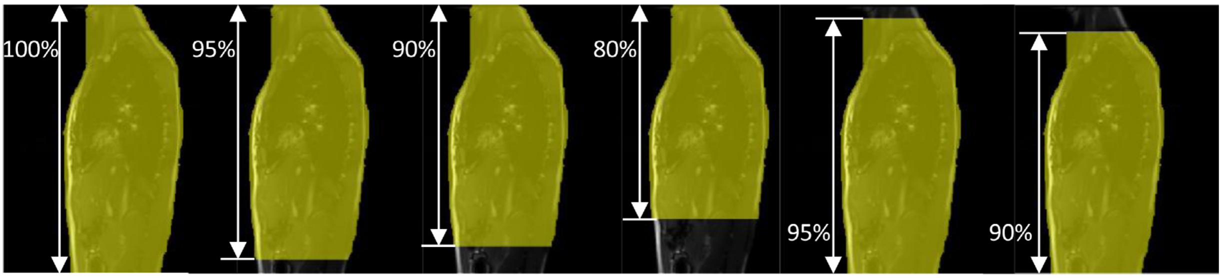

(a) $R0$ (b) $R1$ (c) $R2$ (d) $R3$ (e) $R4$ (f) $R5$

Fig. 12. Different body region definitions. $R0$ is the original R_i. $R1$-$R3$ crop the bottom part of $R0$ by 5%, 10% and 20% according to the height of $R0$. $R4$-$R5$ crop the top part of $R0$ by 5% and 10% according to the height of $R0$. $R0$-$R5$ represent the entire trimmed body region within the skin boundary. The cropped MRI slice together with the segmented binary body region displayed as an overlay is shown for each case of cropping.

(i) P_{NC} – Percentage of correctly identified normal cycles in the filtered set of cycles: Not all normal cycles at each z location are required, and in principle a few or even one normal cycle is sufficient for obtaining 4D constructions. Yet, abnormal cycles may affect our 4D construction results especially if they are grossly abnormal. Therefore, P_{NC} is an important indicator of the effectiveness of the filtration process.

(ii) E_{ie} – Error in detecting EI and EE time points: For a given detected EE (correspondingly EI) time point t in a time sequence A_z, we define the error in its detection $E_{ie}(t)$ as its distance (in terms of the number of time points) from the closest true EE (correspondingly true EI) time point.

(iii) E_{to} – Error in temporal order: This metric defines the number of time instances in a cycle that are out of cyclic order as a fraction of the total number of time instances in the cycle.

(iv) E_{ss} – Degree of spatial smoothness: This metric defines spatial smoothness in the z dimension of the constructed 4D image. For each time-instance of the 4D image, we select one point at the middle of the hemi-diaphragm dome manually. These points will form a curve as a function of z. The smoothness of this curve reflects the spatial continuity quality along z of our 4D construction. To quantify this smoothness, we first fit a spline function to the curve and then use the mean of the absolute distance from the labeled points to the fitted curve as the smoothness factor E_{ss} for that time point.

(v) E_{sc} – Degree of spatial continuity: This metric is similar to E_{ss} except that it is determined via a reader study wherein a reader assigned a spatial smoothness score E_{sc} on a 1 to 5 scale with the following meaning: 1 = the diaphragm region is non-smooth overall; 2 = the diaphragm region at more than 3 locations is non-smooth; 3 = the diaphragm region at 2–3 locations is not smooth; 4 = the diaphragm region at only 1 location is potentially out of order; 5 = the diaphragm region is smooth overall. A score is determined for each time point by visualizing all z-location slices and checking the smoothness of both hemi-diaphragm regions.

4.1. Influence of body region on detecting EE and EI time points

We cropped the size of R_i (Fig. 12) to study how this may influence the error E_{ie} in detecting EE and EI time points. For each cropping condition, we perform the EI and EE detection experiment for all 25 normal pediatric subjects, and obtain the mean and standard deviation (SD) of the E_{ie} value over all subjects, listed in Table 1, and for each subject, depicted graphically in Fig. 13. The true locations of EE and EI points for all cycles (~10,000) were determined by a trained technician.

Table 1
Error in detecting EI and EE time points (E_{ie}) for 25 normal pediatric subjects with different body regions $R0$-$R5$.

	$R0$	$R1$	$R2$	$R3$	$R4$	$R5$
Mean	0.250	0.248	0.244	0.235	0.253	0.252
SD	0.055	0.053	0.053	0.051	0.057	0.057

As can be seen from the results, the mean E_{ie} value for each trimmed case is ~0.25 which is much less than 1 time point. Additionally, for $R0$-$R3$, when the region contains less of the lower abdomen, the results seem to get a little better. This is perhaps now due to our focus on the real motion of interest. This analysis vividly demonstrates that the flux estimated from body region R_i is a robust means of tracking respiratory motion.

4.2. Evaluation of the robustness of the method of filtering cycles

There are three key factors defining the filtering process: the form of loss functions L_1-L_4, weights w_1-w_4, and threshold $\theta 2$. We will examine these factors in turn in relation to filter robustness.

4.2.1. Choice of loss function models

In this section, we will demonstrate that the cycle filtration process is robust and not very sensitive to the elaborate designs by replacing the models used in the four loss functions expressed in Eqs. (7)–(18) by simple linear counterparts, as illustrated in Fig. 9. We will employ metric P_{NC} to compare the accuracies of the two filtering processes. Here again, we established the ground truth by labeling all cycles from 25 normal pediatric subjects (~10,000 cycles) manually as "normal" or "abnormal".

In general, loss functions L_1-L_4 can be replaced by any other forms, including linear. As long as we comply with *Rule* 1 - *Rule* 4, we basically obtain the same results. Eqs. (20)-(23) show the linear counterparts, denoted L'_1, …, L'_4, which we arrived at by following *Rule* 1 - *Rule* 4.

$$L'_1(x) = \begin{cases} \frac{10x}{7} \text{ when } x \geq 0 \\ -\frac{3x}{10} \text{ when } x < 0, \end{cases} \tag{20}$$

$$L'_2(x) = \frac{x}{2} - 1, \tag{21}$$

$$L'_3(x) = 5x, \tag{22}$$

$$L'_4(x) = \begin{cases} \frac{x-2}{4} \text{ when } x \geq 1.5 \\ \frac{1-x}{4} \text{ when } x < 1.5. \end{cases} \tag{23}$$

When using loss functions L_1-L_4, P_{NC} obtained over all 25 pediatric subjects was 98.88%, and for linear loss functions L'_1-L'_4,

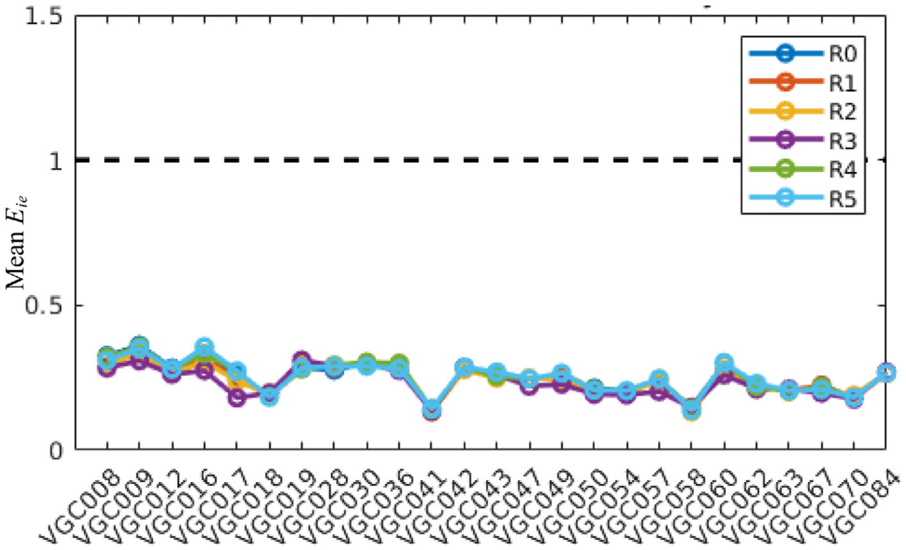

Fig. 13. Error in detecting EI and EE time points. Mean E_{ie} value over the cycles in each data set for 25 normal pediatric subjects with different body region definition ($R0$, $R1$, $R2$, $R3$, $R4$, $R5$).

P_{NC} = 96.79%. This demonstrates that the filtering process is not sensitive to parameters in L_1-L_4 and is indeed very robust. The refined designs based on L_1-L_4 not only make the results a little better, but also make the method conceptually sounder.

4.2.2. Choice of weights w_1-w_4

In the design of L_1-L_4, 0 is the ideal value and 1 is the normalized tolerable boundary value. Therefore, when weighting the loss functions, we should not change their scale. The sum of w_1-w_4 should be equal to 1. These four parameters are set according to the importance of the 4 rules *Rule* 1-*Rule* 4. From our observation, we found that the actual settings did not matter much once the spirit of the above meaning is satisfied. We varied the weights within this meaningful range, like [0.4, 0.2, 0.2, 0.2], and found that the resulting P_{NC} over the 25 pediatric subjects changed from 98.88% to 98.15%, suggesting that once their relative meaning is maintained, the actual value chosen is not very sensitive to the result.

4.2.3. Threshold $\theta 2$

The role of $\theta 2$ is to filter out the abnormal cycles via thresholding the loss L(c). Since we have normalized the tolerable boundary of L(c) to 1, $\theta 2$ should be set between 0 and 1. Due to the complexity of human breathing patterns, 1 is really a fuzzy boundary. When $\theta 2$ is closer to 0, our attitude is conservative which yields higher P_{NC}, but the total number of filtered normal cycles (N_{NC}) may be less. Conversely, when $\theta 2$ is closer to 1, we are more liberal which leads to more filtered cycles (N_{NC}), but P_{NC} itself may be lower. $\theta 2$ is a trade-off between P_{NC} and N_{NC}. For the 4D construction process, as we pointed out, all normal cycles are not really needed, and a few or even one normal cycle per z location can yield good results, although abnormal cycles may affect the final results. Therefore, P_{NC} (accuracy of normal cycle detection) is more important than N_{NC}. Hence, we select $\theta 2$ as 0.4 to keep P_{NC} at a high level. The relationship between P_{NC} and $\theta 2$ for the 25 subjects is depicted in Fig. 14. We can see that 0.4 is a good choice to keep high precision of detecting normal cycles.

Experiments, Results, and Discussion

We tested OFx on dMRI data sets from 25 normal pediatric subjects and 58 pediatric patients with TIS; see Section 2.1 for details on data sets. To evaluate the accuracy of the 4D construction process from different perspectives, we employ the four metrics described in Section 4: E_{ie}, E_{to}, E_{ss}, and E_{sc}.

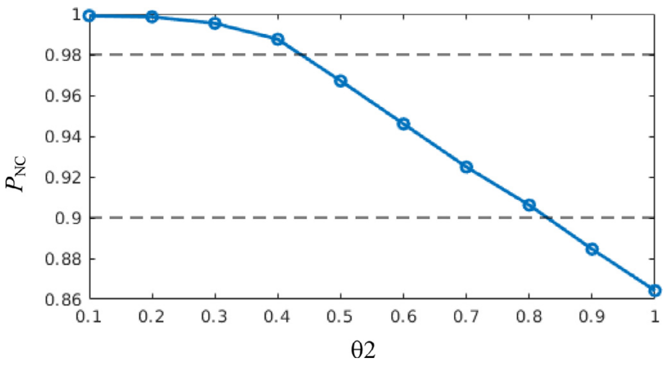

Fig. 14. Variation of P_{NC} as a function of $\theta 2$.

(i) E_{ie}: Error in detecting EI and EE time points

The true locations of EE and EI points for all ~29,000 cycles (83 dMRI data sets × 35 z-locations × 10 cycles per location) were determined by a trained technician by visualizing an animation of the cine sequence A_z. Since our interest is only in normal cycles, we focus on them for evaluating E_{ie}. To understand the distribution of normal and abnormal cycles in our data sets, we display in Fig. 15 these numbers separately for the normal pediatric subjects and TIS patients. A considerable fraction of the total number of cycles is constituted by abnormal cycles – 9.92% for normal data sets and 11.27% for the patient data sets. The number of normal cycles detected per z-location for the two data sets is 2 to 16 with a mean value of 11.2 for normal subjects and 1 to 20 with a mean value of 11.4 for patients. Fig. 16 summarizes E_{ie} values for the two data sets separately. The mean and standard deviation of E_{ie} over all data sets are found to be 0.25 ± 0.05 and 0.38 ± 0.16, respectively, for the two subject groups.

(ii) E_{to}: Error in temporal order

This metric defines the number of time instances in a cycle that are out of cyclic order as a fraction of the total number of time instances in the cycle. In the examples shown in Fig. 17, all cycles

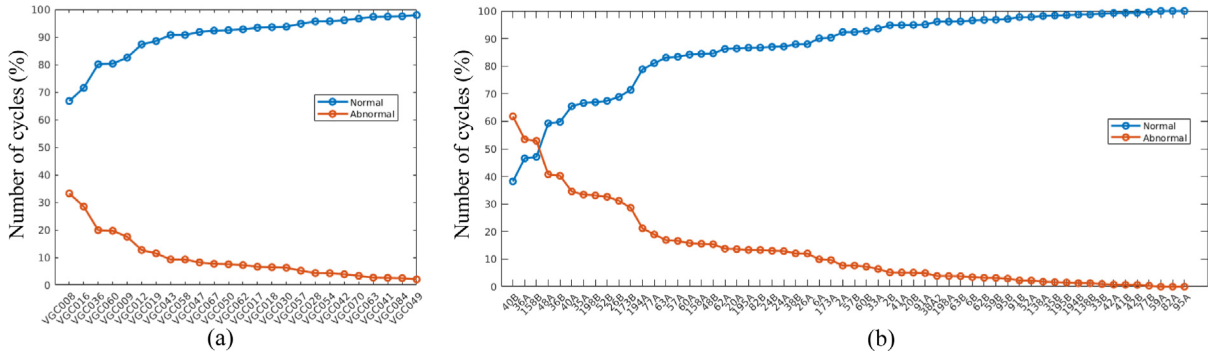

(a) (b)

Fig. 15. Distribution of normal and abnormal cycles in our data sets: (a) normal subjects and (b) TIS patients. Subjects and patients are ordered along the x-axis according to increasing number of normal cycles.

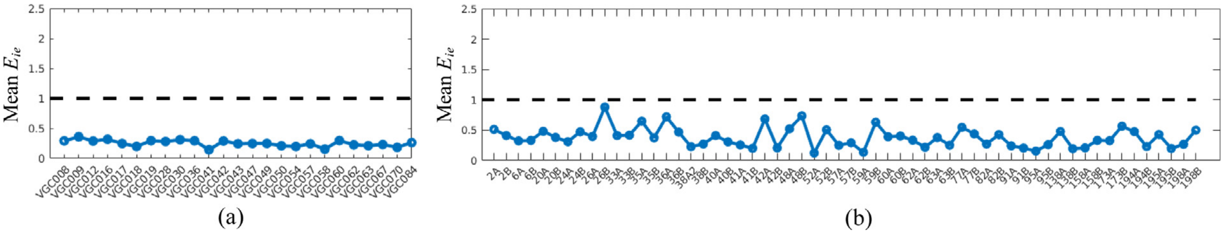

(a) (b)

Fig. 16. Error in detecting EI and EE time points. Mean E_{ie} value over the cycles in each data set for (a) normal pediatric subjects and (b) TIS patients.

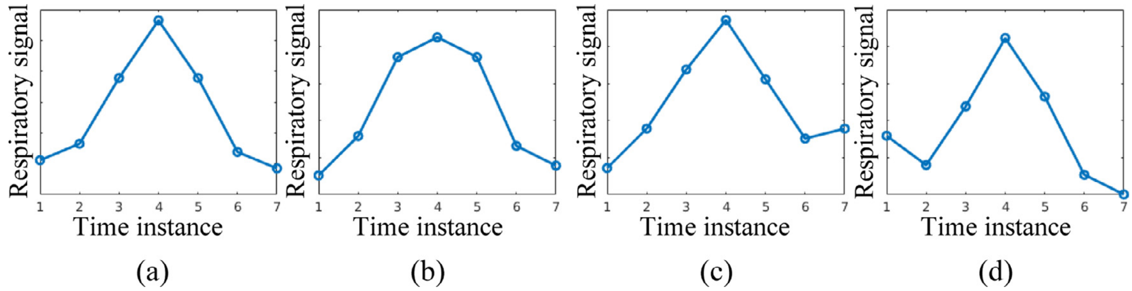

(a) (b) (c) (d)

Fig. 17. Examples of temporal order/ disorder. The cycles in (a) and (b) are in cyclic order. The cycle is out of order at time instance 6 in (c) and at 2 in (d).

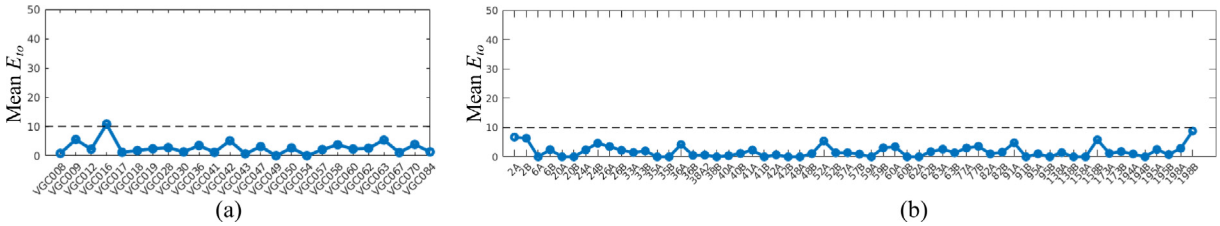

(a) (b)

Fig. 18. Error in temporal order. Mean value of E_{to} over the cycles in in each data set for (a) normal pediatric subjects and (b) TIS patients.

have 7 time instances and 6 time intervals, the cycles in (a) and (b) have all of their time intervals in the proper cyclic order, hence $E_{to} = 0$, and the cycles in (c) and (d) have 1 interval out of order – intervals 6 in (c) and 2 in (d) – and thus $E_{to} = 1/6$ for these cycles. Fig. 18 summarizes E_{to} values for the two data sets separately. The mean and standard deviation of E_{to} over all data sets are found to be 2.7% % 2.3% and 1.8% % 2%, respectively, for the two groups.

(iii) E_{ss}: Degree of spatial smoothness

This metric defines spatial smoothness in the z dimension of the constructed 4D image. For each time-instance of the 4D image, we select one point at the middle of the hemi-diaphragm dome manually. These points will form a curve as a function of z. The smoothness of this curve reflects the spatial continuity quality along z of our 4D construction. To quantify this smoothness, we first fit a spline function to the curve and then use the mean of the absolute distance from the labeled points to the fitted curve as the smoothness factor E_{ss} for that time point. Two examples are shown in Fig. 19 for one time-instance– (a) with $E_{ss} = 0.226$, and (b) with $E_{ss} = 2.422$ (both in pixel units). Note that in each example, for anatomic accuracy, the right hemi-diaphragm appears on the left in the graph, the left hemi-diaphragm appears on the right, and the graph depicts roughly the shape of the hemi-diaphragms at the selected time point in a coronal section corresponding to the chosen mid-point. Fig. 20 demonstrates the mean of E_{ss} values over all time instances for each constructed 4D image for normal subjects and patients in our cohort. Several large spikes seen in Fig. 20(b) corresponding to patients 20B, 41A, 59B, 173A, and 198B happen to be due to patient movement during scanning. Notably our method of evaluation caught those poor scan cases correctly.

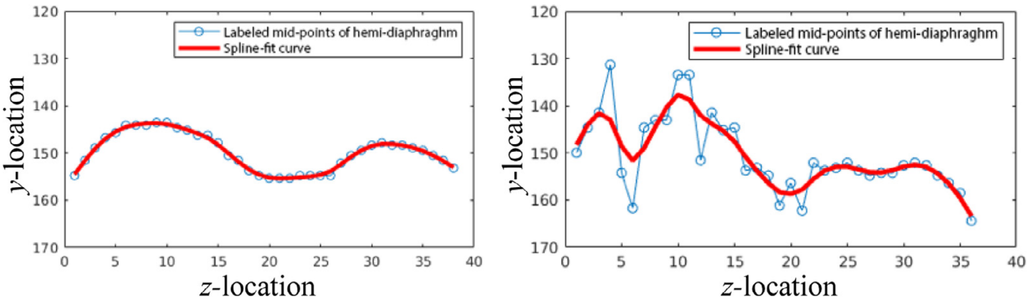

(a) (b)

Fig. 19. Pattern of change in the y-location of the mid-point in the right and left hemi-diaphragm domes: An example of a spatially smooth (a) and non-smooth (b) construction.

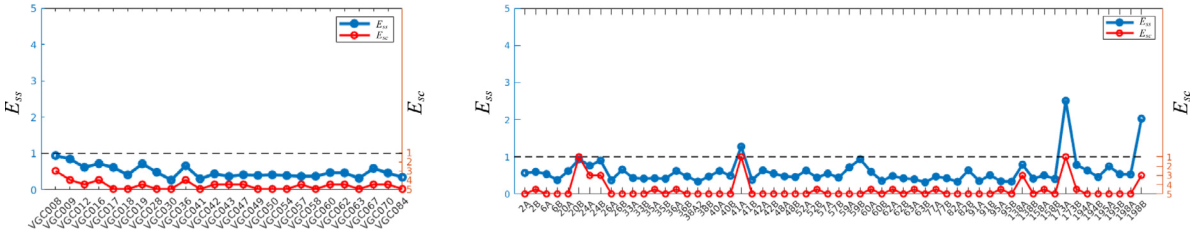

(a) (b)

Fig. 20. Degree of spatial smoothness. Mean of E_{ss} values (blue) and E_{sc} values (red) over all time instances in the constructed 4D image for each normal subject (a) and TIS patient (b) in our data cohort.

Excluding these poor scan cases, the mean and standard deviation of E_{ss} values over all data sets are found to be 0.50 ± 0.17 and 0.54 ± 0.25, respectively, for the two subject groups.

(iv) E_{sc}: Spatial smoothness score

This metric is similar to E_{ss} except that it is determined via a reader study wherein a reader assigned a spatial smoothness score E_{sc} on a 1 to 5 scale with the following meaning: 1 = the diaphragm region is non-smooth overall; 2 = the diaphragm region at more than 3 locations is non-smooth; 3 = the diaphragm region at 2-3 locations is not smooth; 4 = the diaphragm region at only 1 location is potentially out of order; 5 = the diaphragm region is smooth overall. A score is determined for each time point by visualizing all *z*-location slices and checking the smoothness of both hemi-diaphragm regions. Fig. 20 displays the mean of E_{sc} values over all time instances for each constructed 4D image for normal subjects and patients. The mean and standard deviation of E_{sc} values over all data sets are found to be 4.6 ± 0.48 and 4.56 ± 0.98, respectively, for the two subject groups.

From the above results (and others not shown), we make the following observations: (i) The range and mean value of the number of time points in the constructed 4D image for the two populations were: [5, 9], 6.6; and [3, 13], 6.4. Thus, with the same imaging protocol, not surprisingly, normal-subject data sets can be constituted with higher temporal resolution than patient data sets. A desirable feature of our approach is that as the number of normal cycles included in the scan increases, the temporal resolution of the constructed image increases. (ii) As observed previously (Sun et al., 2019), manual labeling itself has a variability of 0.34 ± 0.66 time instances, and thus, our E_{ie} results statistically have a variability of 0.34 ± 0.15, which is statistically the same (p = 0.98) as that from the reference manual method in locating EI and EE time points. Understandably, E_{ie} for normal data sets is less than that for TIS patients with statistical significance (p = 0.0002) due to the higher complexity of the cycles in the latter data sets. (iii) The temporal order seems to be equally accurate in the two subject groups (E_{to} is statistically indistinguishable, p = 0.08) notwithstanding the fact that the cycles in patients are more complex. This is largely due to the accuracy of our detected normal cycles and the method of forming one composite cycle using the model. (iv) Spatial continuity as determined computationally (E_{ss}) and manually (E_{sc}) correlate exceptionally well (Pearson correlation = -0.74) suggesting that the computational method behind metric E_{ss} is valid. The deviation of the estimated *y*-positions of the hemi-diaphragm domes from a smooth fit is much less than one pixel as suggested by E_{ss}.

Finally, in Figs. 21 and 22, we present exemplary slices from a constructed 4D image of a normal subject and a TIS patient. To save space, only selected slices through the right and left lung (*z*-locations) are shown but with the full temporal resolution achieved in the 4D construction. Two video sequences representing visualizations of one 4D constructed image are available at here[4] (a normal pediatric subject). The first video animates the dynamics for each *z*-location over the respiratory cycle of the 4D image and then loops over the *z*-locations. The second video animates the spatial variation in the *z*-direction for each fixed time instance and then loops over the time instances over the respiratory cycle.

Applicability to dynamic CT (dCT): To test the applicability of OFx to dCT images, we performed 4D construction on a dCT data set gathered from a rabbit in connection with a small animal model we have been studying to understand the phenomenon underlying TIS (Tong et al., 2019). The respiratory rate of the rabbit was 37 cycles per minute, the orientation of the slice plane was sagittal with a total of 124 sagittal locations, and the acquisition rate of the slices was at 285 ms per slice for a total of 20 time samples acquired in the time dimension. OFx was applied unmodified to this data set except for threshold $\theta 1$ set to 800 to account for the different modality. OFx successfully constructed a 4D im-

---

[4] http://www.mipg.upenn.edu/Vnews/Materials/4D_video_sequences.pptxhttp://www.mipg.upenn.edu/Vnews/Materials/4D_video_sequences.pptxhttp://www.mipg.upenn.edu/Vnews/Materials/4D_video_sequences.pptx

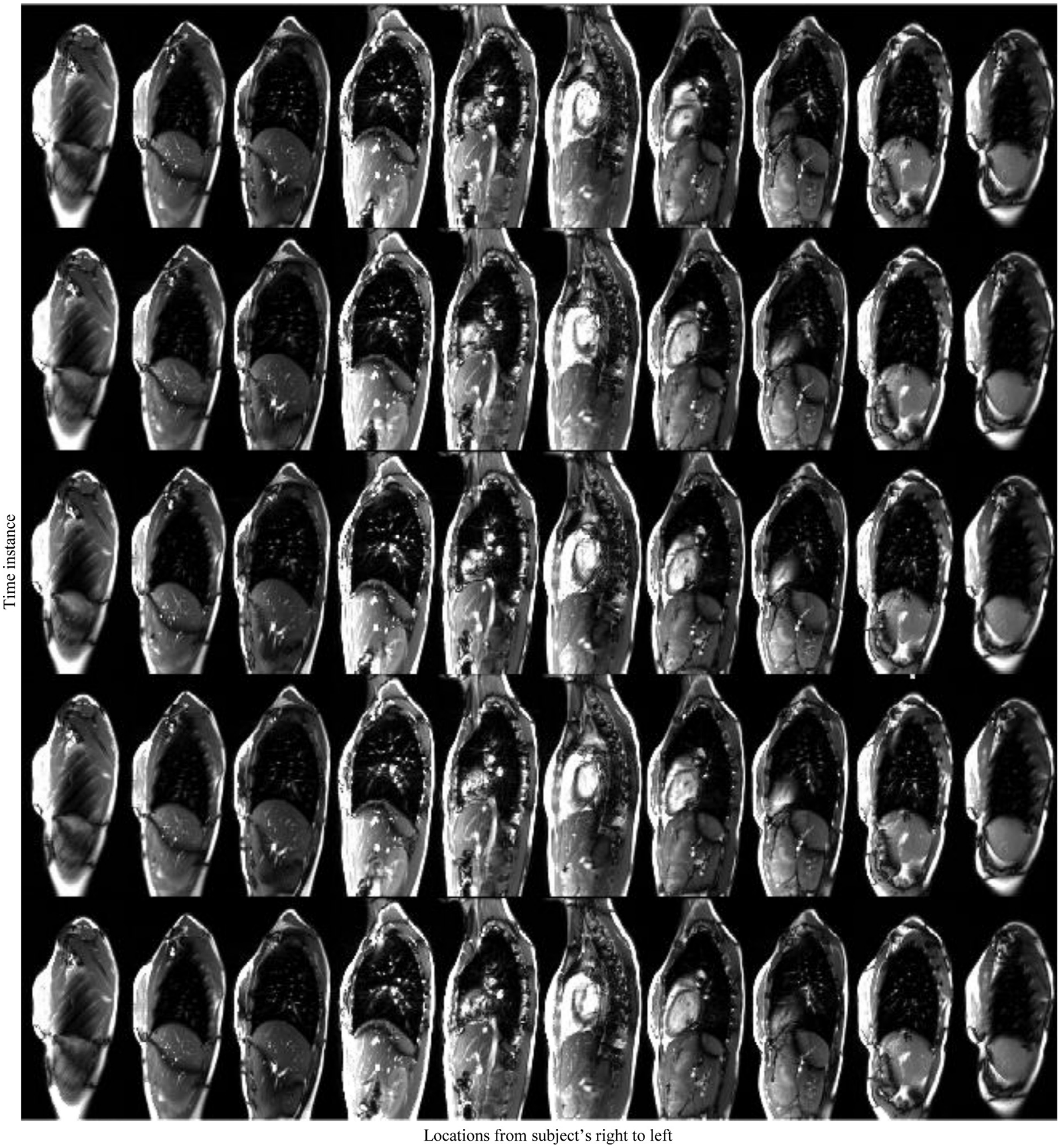

Fig. 21. A display of slices selected from a constructed 4D image of a normal pediatric subject. Each column represents a z-location, and each row represents a time instance.

age with the following error metric values: $E_{ie} = 0.26$; $E_{to} = 1.77\%$; $E_{ss} = 0.19$; and $E_{sc} = 5$. Analogous to Fig. 21 and 22, we display in Fig. 23 some sample slices from the 4D constructed image for the right and left lung.

Computational considerations: The computational time taken per study for our method on a computer with Intel Core i7-8700 is as follows: Step 1 – Respiratory signal extraction: ~321 s; Step 2 – Analysis of cycles: 0.59 s; Step 3 – 4D image formation: 0.02 s. Thus, the total time for fully automated 4D construction from one dMRI scan data set is ~322 s.

Comparison with other methods: The only published methods that we are aware of that operate fully automatically on free breathing slice acquisition data are (Clough et al., 2018; Georg et al., 2008; Vázquez Romaguera et al., 2019; Wachinger et al., 2012). The method in (Vázquez Romaguera et al., 2019) extracts an ROI based on knowledge on the spatial distribution of the organ within the image, which is not robust for slices in patients with abnormal cycles. Methods in (Clough et al., 2018; Georg et al., 2008; Wachinger et al., 2012) extract respiratory signal based on manifold learning, but do not filter the abnormal cycles before alignment, which makes them susceptible to outlier cycles. Among published works, only (Tong et al., 2017) has demonstrated its ability to handle free-breathing dMRI acquisitions from pediatric subjects, as compared to dCT from adult subjects addressed by all other approaches. These two factors are crucial since the challenges in handling pediatric dMRI are much harder than those for adult dCT due to lower image quality and the increased complexity of the respiratory cycles. There are several key differences between our approach and that described in (Tong et al., 2017). (i) (Tong et al., 2017) requires manually identifying EI and

Fig. 22. A display of slices selected from a constructed 4D image of a TIS patient. Each column represents a z-location, and each row represents a time instance.

EE time points first on all A_z sequences which requires a substantial amount of human time. (ii) It formulates a weighted graph where space and time continuity are nested to solve the optimization problem of finding the best 4D volume. Due to this nesting, it cannot handle data sets when only a few slices at sparse z-locations are acquired. Such acquisitions are often helpful for estimating tidal volumes for patients who cannot tolerate long scan times required by full scans. (iii) It does not identify and filter out abnormal cycles, and hence, abnormal cycles in the data can affect the quality of the constructed 4D image or such data sets have to be simply discarded. (iv) The proposed approach has two desirable properties which are not shared by (Tong et al., 2017): First, as already pointed out, the temporal resolution of the constructed image increases with the number of normal cycles in the data set. Second, the existence of the theoretical property mentioned in Section 3, namely the image constructed from a sparse scan is a subimage of the image constructed from a full scan. In summary, the proposed method has several strong features which are unique and make it stand out among currently available approaches for 4D construction.

Concluding Remarks

In this paper, we present a novel approach, named OFx, for automatic 4D image construction from dynamic free-breathing MRI acquisitions of the thorax based on the central concept of *optical flux*. We believe that optical flux is highly correlated with the volume of actual gas exchange and hence acts as an accurate and powerful respiratory surrogate. The method has the following unique features. (i) It is fully automatic while not sacrificing robustness to other impediments such as abnormal breathing patterns. (ii) It is general. With minor changes (mainly relating to body region identification), it can be applied to other modalities such as CT and other MRI protocols. It is not specific to the TIS application illustrated in this work. With some changes, it can also be applied to other dynamic and moving organs such as heart, upper airways, abdominopelvic, and musculoskeletal structures. (iii) The 4D construction principle is independent of the number of z-locations, which implies that it can be employed even when imaging is done to gather only partial data and not the full set across the chest, body region, or organ of interest. Recovering spatial continuity based on guaranteed temporal continuity is the fundamental premise of this approach. (iv) It has two desirable theoretical properties – the image constructed from partial data being a subimage of the image constructed from full data; and the temporal resolution increasing with the number of normal cycles included in the scan. In fact, as the dMRI temporal resolution increases, in the limit, OFx would converge to a perfect solution.

It should be noted that OFx is different from methods that employ body region area to derive a surrogate for respiratory signal. The area measure is sensitive to errors in segmentation of the region and may require some user interactive help. Optical flux is insensitive to segmentation errors and is actually a measure of the body motion due to respiration, not just of the outer skin surface but also of the internal structures including the chest wall and diaphragm. Structures with greater motion make correspondingly larger contributions to optical flux. An underpinning of OFx is that it first ensures time continuity and then restores spatial continuity while preserving time continuity. During normal breathing, the motion depicted in A_z for different z will be similar. Therefore, the effectiveness of OFx will be guaranteed once similar normal cycles are detected and the phase for each time instant in each cycle is accurately identified.

One current gap in OFx is that if a time series A_z does not contain any normal cycles (or if the method fails to find any such cycles when the series actually contains normal cycles), it will fail

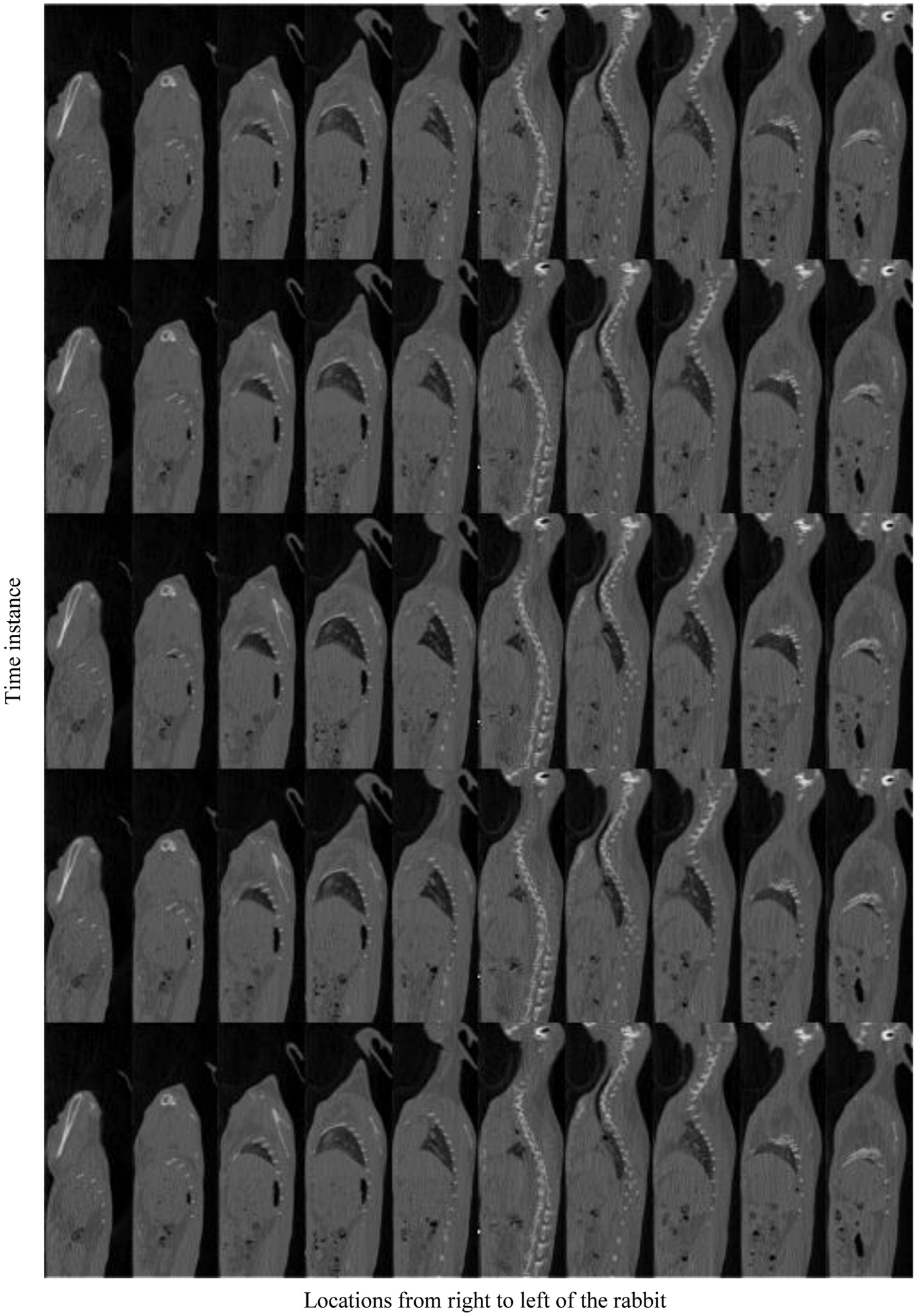

Fig. 23. A display of slices selected from the constructed 4D image of a rabbit. Each column represents a z-location, and each row represents a time instance.

to form a 4D image. In our analysis of all 83 data sets, however, we did not encounter such a situation. Second, we believe that the cycle filtering approach may perhaps be improved via the use of deep networks such as Long Short-Term Memory (LSTM) (Hochreiter and Schmidhuber, 1997) which may help in salvaging some near-normal cycles which our current rather conservative approach may fail to detect. Third, the cosine function utilized by OFx may not be suitable to model a normal breathing cycle since the inspiration and expiration phases are known not to be identical in length. Notably, OFx is not dependent on the specific cosine function and so other more appropriate non-symmetric functions such as a Rayleigh distribution (Wait, 1985) can be utilized in the future.

Our future goal is to adapt OFx to other modalities, body regions, organs, populations, and applications.

Declaration of Competing Interest

The authors declare that they have no known competing financial interests or personal relationships that could have appeared to influence the work reported in this paper.

CRediT authorship contribution statement

You Hao: Conceptualization, Methodology, Software, Validation, Formal analysis, Investigation, Writing - original draft, Project administration, Visualization. **Jayaram K. Udupa:** Conceptualization, Methodology, Validation, Formal analysis, Investigation, Resources, Data curation, Writing - review & editing, Supervision, Project administration, Funding acquisition. **Yubing Tong:** Conceptualization, Software, Validation, Formal analysis, Investigation, Resources, Data curation, Writing - review & editing, Project administration. **Caiyun Wu:** Validation, Data curation. **Hua Li:** Writing - review & editing. **Joseph M. McDonough:** Data curation, Writing - review & editing. **Carina Lott:** Data curation. **Catherine Qiu:** Data curation. **Nirupa Galagedera:** Data curation. **Jason B. Anari:** Data curation. **Drew A. Torigian:** Resources, Data curation, Writing - review & editing. **Patrick J. Cahill:** Resources.

Acknowledgement

This research is supported partly by a “Frontier Grant” from The Children’s Hospital of Philadelphia, an NIH grant R01HL150147, and an ITMAT MHB grant from University of Pennsylvania. The authors are grateful to Dr. Casey Olson for the rabbit data set utilized for demonstrating the applicability of the OFx method to the CT modality. The training of Mr. You Hao in the Medical Image Processing Group is supported by a scholarship from China Scholarship Council. We thank Dewey Odhner for his help on data processing with the CAVASS software system.

References

Baumgartner, C.F., Gomez, A., Koch, L.M., Housden, J.R., Kolbitsch, C., McClelland, J.R., Rueckert, D., King, A.P., 2015. Self-aligning manifolds for matching disparate medical image datasets, in: Information Processing in Medical Imaging. pp. 363–374. https://doi.org/10.1007/978-3-319-19992-4_28

Baumgartner, C.F., Kolbitsch, C., Balfour, D.R., Marsden, P.K., McClelland, J.R., Rueckert, D., King, A.P., 2014. High-resolution dynamic MR imaging of the thorax for respiratory motion correction of PET using groupwise manifold alignment. Med. Image Anal. 18 (7), 939–952. doi:10.1016/j.media.2014.05.010.

Baumgartner, C.F., Kolbitsch, C., McClelland, J.R., Rueckert, D., King, A.P., 2013. Groupwise simultaneous manifold alignment for high-resolution dynamic MR imaging of respiratory motion, in: Information Processing in Medical Imaging. pp. 232–243. https://doi.org/10.1007/978-3-642-38868-2_20

Cai, J., Chang, Z., Wang, Z., Paul Segars, W., Yin, F.F., 2011. Four-dimensional magnetic resonance imaging (4D-MRI) using image-based respiratory surrogate: a feasibility study. Med. Phys. 38 (12), 6384–6394. doi:10.1118/1.3658737.

Campbell Jr, R.M., Smith, M.D., 2007. Thoracic insufficiency syndrome and exotic scoliosis. J. Bone Jt. Surg. Am 89 (Suppl. 1), 108–122. doi:10.2106/00004623-200701001-00013.

Campbell Jr., R.M., Smith, M.D., Mayes, T.C., Mangos, J.A., Willey-Courand, D.B., Kose, N., Pinero, R.F., Alder, M.E., Duong, H.L., Surber, J.L., 2003. The characteristics of thoracic insufficiency syndrome associated with fused ribs and congenital scoliosis. J. Bone Jt. Surg. Am 85 (3), 399–408. doi:10.2106/00004623-200303000-00001.

Chen, X., Usman, M., Baumgartner, C.F., Balfour, D.R., Marsden, P.K., Reader, A.J., Prieto, C., King, A.P., 2017. High-resolution self-gated dynamic abdominal MRI using manifold alignment. IEEE Trans. Med. Imaging 36 (4), 960–971. doi:10.1109/TMI.2016.2636449.

Clough, J.R., Balfour, D.R., Marsden, P.K., Prieto, C., Reader, A.J., King, A.P., 2018. MRI slice stacking using manifold alignment and wave kernel signatures. In: International Symposium on Biomedical Imaging, pp. 319–323. doi:10.1109/ISBI.2018.8363583.

Crompton, G., 2006. A brief history of inhaled asthma therapy over the last fifty years. Prim. Care Respir. J. 15 (6), 326–331. doi:10.1016/j.pcrj.2006.09.002.

Crooke, P.S., Marini, J.J., Hotchkiss, J.R., 2002. Modeling recruitment maneuvers with a variable compliance model for pressure controlled ventilation. J. Theor. Med. 4 (3), 197–207. doi:10.1080/1027366021000023124.

Deng, Z., Pang, J., Yang, W., Yue, Y., Sharif, B., Tuli, R., Li, D., Fraass, B., Fan, Z., 2016. Four-dimensional MRI using three-dimensional radial sampling with respiratory self-gating to characterize temporal phase-resolved respiratory motion in the abdomen. Magn. Reson. Med. 75 (4), 1574–1585. doi:10.1002/mrm.25753.

Georg, M., Souvenir, R., Hope, A., Pless, R., 2008. Manifold learning for 4D CT reconstruction of the lung. In: 2008 IEEE Computer Society Conference on Computer Vision and Pattern Recognition Workshops, pp. 1–8. doi:10.1109/CVPRW.2008.4563024.

Hochreiter, S., Schmidhuber, J., 1997. Long short-term memory. Neural Comput 9 (8), 1735–1780. doi:10.1162/neco.1997.9.8.1735.

Karani, N., Zhang, L., Tanner, C., Konukoglu, E., 2019. An image interpolation approach for acquisition time reduction in navigator-based 4D MRI. Med. Image Anal. 54, 20–29. doi:10.1016/j.media.2019.02.008.

Korn, G.A., Korn, T.M., 2000. Mathematical handbook for scientists and engineers: definitions, theorems, and formulas for reference and review. Courier Corporation.

Liu, Y., Yin, F.F., Chang, Z., Czito, B.G., Palta, M., Bashir, M.R., Qin, Y., Cai, J., 2014. Investigation of sagittal image acquisition for 4D-MRI with body area as respiratory surrogate. Med. Phys. 41 (10), 101902. doi:10.1118/1.4894726.

Liu, Y., Yin, F.F., Chen, N.K., Chu, M.L., Cai, J., 2015. Four dimensional magnetic resonance imaging with retrospective k-space reordering: a feasibility study. Med. Phys. 42 (2), 534–541. doi:10.1118/1.4905044.

Low, D.A., Parikh, P.J., Lu, W., Dempsey, J.F., Wahab, S.H., Hubenschmidt, J.P., Nystrom, M.M., Handoko, M., Bradley, J.D., 2005. Novel breathing motion model for radiotherapy. Int. J. Radiat. Oncol. Biol. Phys. 63 (3), 921–929. doi:10.1016/j.ijrobp.2005.03.070.

Lucas, B.D., Kanade, T., 1981. An iterative image registration technique with an application to stereo vision. In: Proceedings of Imaging Understanding Workshop, pp. 121–130.

Maxwell, J.C., 1881. A treatise on electricity and magnetism, 2nd ed. Clarendon Press.

Mols, G., Brandes, I., Kessler, V., Lichtwarck-Aschoff, M., Loop, T., Geiger, K., Guttmann, J., 1999. Volume-dependent compliance in ARDS: Proposal of a new diagnostic concept. Intensive Care Med 25 (10), 1084–1091. doi:10.1007/s001340051016.

Quanjer, P.H., Tammeling, G.J., Cotes, J.E., Pedersen, O.F., Peslin, R., Yernault, J.C., 1993. Lung volumes and forced ventilatory flows. Eur. Respir. J. 6 (Suppl. 16), 5–40. doi:10.1183/09041950.005s1693.

Remmert, G., Biederer, J., Lohberger, F., Fabel, M., Hartmann, G.H., 2007. Four-dimensional magnetic resonance imaging for the determination of tumour movement and its evaluation using a dynamic porcine lung phantom. Phys. Med. Biol. 52 (18). doi:10.1088/0031-9155/52/18/N02, N401–N415.

Sun, C., Udupa, J.K., Tong, Y., Wu, C., Guo, S., McDonough, J.M., Torigian, D.A., Campbell, R.M., 2019. Auto-labeling of respiratory time points in free-breathing thoracic dynamic MR image acquisitions for 4D image construction. In: Proc. SPIE 10953, Medical Imaging 2019: Biomedical Applications in Molecular. Structural, and Functional Imaging doi:10.1117/12.2513218, 109531B.

Tong, Y., Udupa, J.K., Ciesielski, K.C., Wu, C., McDonough, J.M., Mong, D.A., Campbell Jr, R.M., 2017. Retrospective 4D MR image construction from free-breathing slice Acquisitions: a novel graph-based approach. Med. Image Anal. 35, 345–359. doi:10.1016/j.media.2016.08.001.

Tong, Y., Udupa, J.K., McDonough, J.M., Wileyto, E.P., Capraro, A., Wu, C., Ho, S., Galagedera, N., Talwar, D., Mayer, O.H., Torigian, D.A., Campbell, R.M., 2019. Quantitative dynamic thoracic MRI: Application to thoracic insufficiency syndrome in pediatric patients. Radiology 292 (1), 206–213. doi:10.1148/radiol.2019181731.

Uh, J., Khan, M.A., Hua, C., 2016. Four-dimensional MRI using an internal respiratory surrogate derived by dimensionality reduction. Phys. Med. Biol. 61 (21), 7812. doi:10.1088/0031-9155/61/21/7812.

Vázquez Romaguera, L., Olofsson, N., Plantefève, R., Lugez, E., De Guise, J., Kadoury, S., 2019. Automatic self-gated 4D-MRI construction from free-breathing 2D acquisitions applied on liver images. Int. J. Comput. Assist. Radiol. Surg. 14 (6), 933–944. doi:10.1007/s11548-019-01941-1.

von Siebenthal, M., Székely, G., Gamper, U., Boesiger, P., Lomax, A., Cattin, P., 2007. 4D MR imaging of respiratory organ motion and its variability. Phys. Med. Biol. 52 (6), 1547–1564. doi:10.1088/0031-9155/52/6/001.

Wachinger, C., Yigitsoy, M., Rijkhorst, E.J., Navab, N., 2012. Manifold learning for image-based breathing gating in ultrasound and MRI. Med. Image Anal. 16 (4), 806–818. doi:10.1016/j.media.2011.11.008.

Wait, J.R., 1985. Electromagnetic wave theory. Harper & Row, New York.

Yang, J., Cai, J., Wang, H., Chang, Z., Czito, B.G., Bashir, M.R., Yin, F.F., 2014. Four-dimensional magnetic resonance imaging using axial body area as respiratory surrogate: Initial patient results. Int. J. Radiat. Oncol. Biol. Phys. 88 (4), 907–912. doi:10.1016/j.ijrobp.2013.11.245.